In vivo cartography of state-dependent signal flow hierarchy in the human cerebral cortex

Seok-Jun Hong
hongseokjun@skku.edu

Sungkyunkwan University https://orcid.org/0000-0002-1847-578X

Younghyun Oh
Sungkyunkwan University

Yejin Ann
Sungkyunkwan University

Jae-Joong Lee
Sungkyunkwan University https://orcid.org/0000-0002-7353-8683

Takuya Ito
IBM Research https://orcid.org/0000-0002-2060-4608

Sean Froudist-Walsh
University of Bristol

Casey Paquola
Forschungszentrum Julich

Michael Milham
Child Mind Institute https://orcid.org/0000-0003-3532-1210

R. Nathan Spreng
McGill University https://orcid.org/0000-0003-1530-8916

Daniel Margulies
Centre National de la Recherche Scientifique (CNRS) https://orcid.org/0000-0002-8880-9204

Boris Bernhardt
2. Department of Neurology and Neurosurgery, McGill University, Quebec, Canada

Choong-Wan Woo
Center for Neuroscience Imaging Research, Institute for Basic Science, Suwon, South Korea
https://orcid.org/0000-0002-7423-5422

Article

Keywords:

Posted Date: October 21st, 2024

DOI: https://doi.org/10.21203/rs.3.rs-5219295/v1

Additional Declarations: There is **NO** Competing Interest.

Abstract

Understanding the principle of information flow across distributed brain networks is of paramount importance in neuroscience. Here, we introduce a novel neuroimaging framework, leveraging integrated effective connectivity (iEC) and unconstrained signal flow mapping for data-driven discovery of the human cerebral functional hierarchy. Simulation and empirical validation demonstrated the high fidelity of iEC in recovering connectome directionality and its potential relationship with histologically defined feedforward and feedback pathways. Notably, the iEC-derived hierarchy displayed a monotonously increasing level along the axis where the sensorimotor, association, and paralimbic areas are sequentially ordered – a pattern supported by the Structural Model of laminar connectivity. This hierarchy was further demonstrated to flexibly reorganize according to brain states, flattening during an externally oriented condition, evidenced by a reduced slope in the hierarchy, and steepening during an internally focused condition, reflecting heightened engagement of interoceptive regions. Our study highlights the unique role of macroscale directed functional connectivity in uncovering a neurobiologically grounded, state-dependent signal flow hierarchy.

Introduction

Human cognition arises from ever-changing dynamical flows of neural information across distributed brain networks. Cortical hierarchy, one of the most fundamental architectures for this functional dynamics, has been extensively investigated in previous studies, with a focus on the computational principles of sensorimotor hierarchies in early work[1–7], while recently more expanded to the whole-brain level[8–10] to highlight its global basis involved in a wide range of cognitive functions. Indeed, a rich array of evidence from histology[11,12], tract-tracing[13,14], and functional MRI (fMRI)[15,16] studies has shown that both human and non-human primate brains exhibit a unique large-scale organizational axis spanning from the sensorimotor to association cortices, termed as 'functional gradient'[9] or 'global processing hierarchy'[9,17,18]. Notably, this macro-scale axis has been reproduced across multiple neuroimaging studies[19–24] and related to multiple cognitive functions such as perception, action and social processing[23,25–27], typical development[21,28,29] and system-level pathogenicity in neuropsychiatric conditions[30–34]. Despite its significance, exactly how the hierarchical organization emerges from dynamical neural information flow remains poorly understood.

Two major issues contribute to this lack of understanding: 1) the state-dependent organization of functional brain dynamics and 2) the limitations of conventional fMRI connectome analytics. The former arises from the brain's frequent state transitions. Indeed, in daily life, our brain continuously shifts between different states, driven by exteroceptive stimuli, such as watching a movie with a high influx of multisensory information, as well as interoceptive signals, such as hunger or thirst reflecting the ongoing physiological states of the body. Even at rest, the brain dynamically organizes neural pathways to generate diverse thoughts from continuous mind wandering. While this "state-dependent functional dynamic" is a fundamental characteristic of the brain for adaptive behaviors, so far only few studies have systematically compared different brain states with respect to their dynamics, especially in the context of information flow along the cortical hierarchy.

The second issue is that the current network neuroscience approach predominantly relies on *undirected* functional connectivity (FC). Given that the brain network is a constellation of feedforward and feedback pathways, the inability to infer connectome directionality significantly impedes the field’s advancement. This challenge has spurred the development of an alternative approach— *effective connectivity* (EC) mapping—a 'directed version' of connectome analytics. This technique, which enables the statistical inference of the net influence of one brain area on another, has been increasingly sophisticated and improved in recent studies, now supporting even the whole-brain assessment of directed connections based on fMRI data[35–37]. As these methods flourish, however, EC research is encountering new challenges related to algorithm development and validation[38], which are crucial to address to move forward to the next generation of EC approaches. These issues are summarized as follows:

1. *Overabundance of EC algorithms*. Over the last two decades, the field has witnessed the proposal of numerous EC algorithms[36,37,39–50], each based on a unique mathematical principle. This diversity, while testament to the field's vibrant interest, paradoxically resulted in a lack of consensus, which made it unclear when and how to use each algorithm and raised concerns for reproducibility of findings[41,49,51–55], as different methodological foundations may lead to unintended variations in the results.
2. *Network complexity*. While different EC methods have unique strengths in their statistical properties, most of them have not been sufficiently tested for high-complexity network data (*e.g.*, high-resolution network nodes with dense cyclic and negative connections), and except for few recent studies[35,36], their scale often remained on the order of several dozen nodes[41,48,56–59]. As shown in recent approaches of brain parcellation, however, the human cerebral cortex can be divided into at least ≥ 100 functionally and/or structurally distinct areas[60,61]. Developing EC algorithms that are scalable to networks with high dimensionality and complexity is therefore imperative to precisely infer the functional dynamics in the human brain.
3. *Lack of biological validation*. EC algorithms are typically validated using artificially simulated networks rather than real biological data. This is particularly true in the human brain, where ground truth remains unknown. This lack of biological validation often leads to a limited use of EC analyses, mainly for those studies having a clear hypothesis on the connectivity configuration of a targeted circuit[62–64] (but see recent advances[65–67]).

Here, we propose a unified imaging analysis framework termed “integrated EC (iEC)” to overcome these challenges. This approach is based on the idea of combining multiple existing EC algorithms with distinct mathematical properties[38] in order to synergize their complementary strengths while obviating the development of yet another statistical algorithm. To implement this, we underwent an extensive validation of individual EC algorithms and integrated them into the iEC framework, testing on the simulation of biologically plausible networks and comparing with the empirical tract-tracing and resting-state fMRI data across two different network complexities, both comprising ≥ 100 nodes and dense cyclic connections.

After demonstrating the significant prediction accuracy of the iEC framework, we used it to thoroughly chart out the characteristics of directed functional connectivity in the human brain. This analysis revealed distinct connectional polarity along the cortical hierarchy, with unimodal sensory areas predominantly sending positive signals, whereas heteromodal association areas exhibit a balanced ratio of positive and negative signals. Given that these patterns closely mirror converging evidence on the characteristics of feedforward and feedback connections in previous studies[68–70], we further leveraged a data-driven method to estimate the hierarchical level based on iEC. This provided, for the first time, a neurobiologically grounded '*signal flow functional hierarchy*' in the human brain. Indeed, this map showed a remarkably similar pattern to a previously established conceptual model of the brain hierarchy (*i.e.*, Mesulam's proposition[71]) but also to cytoarchitecturally determined cortical types[72], both spanning from low-level sensory (koniocortical) to higher-order (eulaminate and dysgranular) areas and up to the paralimbic (agranular) regions, the latter mainly known for interoceptive cortical areas that relay signals from the 'internal milieu' (*i.e.* body and organs)[73]. Lastly, we demonstrated that the identified cortical hierarchy undergoes considerable state-dependent reorganization by comparing the hierarchy map of the resting state to those of two other (non-resting) brain states, *i)* a movie-watching condition which mainly evokes externally oriented process, and *ii)* a tonic pain condition (induced by oral capsaicin), which evokes more interoceptive bodily sensation. Together, our iEC framework offers a unique opportunity for *in-vivo* cartography of signal flow hierarchy in the human brain and paves a way towards a quantitative delineation of state-dependent network information flow.

Results

Our study consists of two main phases. First, we examined the distinct characteristics of individual EC algorithms. While investigating the strengths and weaknesses of each method, we developed a new approach to integrate their results (integrated EC, hereafter called 'iEC'), which demonstrated significantly improved accuracy of EC mapping through a multi-step validation process. In the second phase, we utilized this iEC to comprehensively examine the human brain in terms of *i)* global patterns of unconstrained signal flows, *ii)* retrieval of signal flow hierarchy, and *iii)* the state-dependent reorganization of this hierarchical structure.

To develop our iEC framework, we first selected representative EC algorithms using a taxonomy created based on predefined methodological criteria (Fig. 1a **and Supplementary Fig. 1;** see **Methods** '*2. Effective connectivity algorithms*' for more details). Specifically, we divided existing EC algorithms into two principal categories: the Graphical model and the Dynamical system. Within each category, we applied specific criteria to ensure *i)* detection of cyclic connections, *ii)* scalability and *iii)* mathematical uniqueness. This process led us to identify three distinct methods, each from a unique algorithmic family: Fast Adjacency Skewness (FASK in the BayesNet family)[41], Vector Autoregressive Model (VAR in the lag-based family)[74] and regression Dynamic Causal Modeling (rDCM in the broader DCM family)[36]. The chosen algorithms were then integrated to construct the iEC. To this end, we computed a weighted sum of individual EC results (*i.e.*, $\mathrm{iEC}=\beta_1\times\mathrm{EC}_{\mathrm{rDCM}}+\beta_2\times\mathrm{EC}_{\mathrm{VAR}}+\beta_3\times\mathrm{EC}_{\mathrm{FASK}}$; Fig. 1b), in which the β value for each algorithm was optimized to yield the iEC such that it shows the highest correlation with the target connectivity metrics (explained in the next section). To prevent overfitting, we optimized the weights in a cross-validated manner, employing Bayesian optimization[75] (see **Methods** '*2.4 Integrated EC framework*').

1. Three-step validation of EC algorithms

To comprehensively evaluate the accuracy of individual algorithms and iEC, we employed a multi-step validation, including *i)* whole-brain simulation using synthetic directed networks, and empirical data comparison using *ii)* non-human primate and *iii)* human brain networks (Fig. 1c). The details are as follows.

1.1 Validation using synthetic networks

To maximize biological plausibility, a group-averaged structural connectivity (SC) from empirical human diffusion MRI data was used as an initial template for synthetic network generation (Fig. 2a). Upon this SC template, we induced directionality by randomly rearranging their connections while preserving each node's outdegree. Then, the Hopf model, a well-established tool for simulating oscillatory neural dynamics[76], was employed to generate brain signals based on these synthetic networks. The signals were then fed into each EC algorithm (*i.e.*, FASK, VAR, and rDCM). The outcomes were compared to the ground truth target matrix (*i.e.*, directed synthetic network) using two representative graph-theoretical metrics: edge strength (*i.e.* connectome-wise EC magnitude) and weighted degree centrality.

The inferred ECs from all individual algorithms demonstrated significant correlations with the synthetic networks, as measured by edge strength (Fig. 2b; r_{median} for rDCM, VAR, and FASK (Schaefer/MMP) = 0.61,0.73,0.74/0.37,0.44,0.54, respectively; $p_{\mathrm{FDR}}<0.001$) and degree distribution (Fig. 2c; r_{median} for rDCM, VAR, and FASK (indegree/outdegree) = 0.38,0.37,0.42/0.42,0.43,0.53 when using MMP; all $p_{\mathrm{FDR}}<0.001$; see **Supplementary Fig. 2** for results from the Schaefer atlas). The accuracies also highlighted unique differences among these algorithms, with FASK outperforming the others in all simulations, particularly in a more complex network that have a higher number of nodes (*i.e.*, MMP-360). Notably, the iEC framework successfully integrated individual algorithms, showing a markedly higher correlation with the ground truths across all metrics and parcellation schemes ($r_{\mathrm{median}}=0.83/0.64$ for edge strength correlation of Schaefer/MMP; $r_{\mathrm{median}}=0.45/0.57$ for degree correlation of Schaefer/MMP; all $p < 0.001$; we further investigated the details of the β value optimization in **Supplementary Fig. 3**).

1.2 Validation using macaque tract-tracing and fMRI data

After initial validation through simulation, we broadened our assessment to include real-world scenarios, employing a tract-tracing[10] and resting-state fMRI (PRIME DE[77]) from the macaque brain (Fig. 2d). We applied the individual EC algorithms to the resting-state fMRI data from 19 anesthetized macaques, parcellated using the M132 atlas[13]. These individual results were then integrated to construct the iEC using the same cross-validation strategy as in the simulation analysis. To evaluate the performance of EC mapping, we compared EC with the “Fraction of Labeled Neurons (FLN)”, an established tract-tracing measure developed in the macaque research community[13]. Specifically, FLN refers to the proportion of neurons that are histologically labeled after tracer injections, which indicates the *directed* connectivity strength between the injected and target regions (see **Methods** ‘*1.1 Macaque tract-tracing data*’ for details).

The quantitative comparison showed that both rDCM and FASK could recover the FLN matrix with a significant accuracy (r_{median}=0.44 and 0.43, respectively; all $p < 0.001$). Corroborating a previous finding from our simulation analysis, the iEC framework outperformed these individual algorithms (r_{median}=0.53, $p < 0.001$), further highlighting the strength and efficacy of our integration approach (Fig. 2e). Notably, visual inspection of iEC results (“Integrated EC” matrix in Fig. 2d) indicated that positive connections (red color-coded) are both stronger and more prevalent, while negative connections (blue color-coded) across the brain areas are generally weak and sparse. Previous studies suggested that these connection polarities from fMRI may reflect intricately mixed excitatory and inhibitory effects[78,79], potentially aligned with feedforward (FF) and feedback (FB) signal pathways[68]. Indeed, while a dominant portion of FF connections have been previously found to target excitatory neurons (thus exerting positive and amplifying influences to target regions)[80], FB connections were associated with both excitatory and inhibitory pathways[81–83], although the later, ‘suppressive’ effect has traditionally been considered a major characteristic of FB. To assess whether these distinct patterns can be also captured in our macro-scale analysis, we profiled the iEC with respect to SLN (Fraction of Supragranular Labeled Neurons), a marker to quantitatively index the level of FF and FB connectivity[84] (see **Methods** ‘*1.1 Macaque tract-tracing data*’). Interestingly, when we categorized iECs into FF or FB by applying 0.5 threshold to their SLN value (range: 0–1; FF: SLN > 0.5; FB: SLN < 0.5), the majority of iECs corresponding to the FF pathway were positive, while those corresponding to FB showed a relatively balanced ratio of positive and negative connections (Fig. 2f), mirroring previous reports on signal influences exerted by FF/FB pathways.

1.3 Validation using human fMRI

Finally, we evaluated the EC algorithms using human resting-state fMRI (from HCP 440-subjects discovery/replication data; see **Methods** *2.4 Integrated EC framework*). As an established ground truth is absent in the human brain, we devised a new evaluation method termed “EC-to-FC recovery” (Fig. 2g). In this approach, the EC inferred by each algorithm was fed into the Hopf model, serving as a virtual backbone of directed connectivity to generate brain signals. This in turn allowed the reconstruction of a simulated FC matrix. We compared this recovered FC with an empirical FC derived from actual fMRI signals (thus '*EC-to-FC recovery*'). The rationale underpinning this approach is that if the inferred EC effectively captures the true underlying net-influence structure of brain network organization, the FC simulated from this EC should reasonably emulate its empirical FC counterpart.

Consistent with our previous validation, testing on the human brain also revealed the effectiveness of our iEC framework, which showed the highest correlation with empirical data (Fig. 2h; $r_{median}=0.75$, $p < 0.001$ at the individual level, and $r_{median}=0.81$, $p < 0.001$ at the group level based on MMP-360; see **Supplementary Fig. 4a** for the result from Schaefer-100). Notably, regarding the performance of individual algorithms, contrary to the findings of previous analyses, FASK showed the lowest accuracy in this setup (EC-to-FC recovery; Fig. 2h). This finding suggests that high EC-identification performance alone (Fig. 2b, e) does not guarantee the effective EC-to-FC recovery, and that more complex interactions among various factors related to the connectivity may be involved (see **Supplementary Fig. 4b** for more details about this issue, where we performed a *post-hoc* analysis scrutinizing the contribution of each algorithm on the EC inference along their connectome properties).

2. Investigation of iEC profiles and signal flow hierarchy in the human brain

2.1 Profiling of the human whole-brain iEC

Having validated our iEC framework, we now focus on the profiling of the human whole-brain EC architecture using a group-level iEC matrix derived from resting-state fMRI of 220 healthy young adults (*i.e.*, discovery dataset).

Organizing the connectivity matrix according to the Yeo-Krienen atlas[85] revealed a distinct connectome organization (Fig. 3a): connections within modules were predominantly positive, while those between modules mainly fell into the negative range, which may reflect a nature of functional interactions in terms of network integration and segregation. Furthermore, in line with previous electrophysiological recording and retrograde tract-tracing experiments[86,87], the ECs in the human brain exhibited a heavy-tailed distribution of connectivity strength (tail index = 1.45; the tail index < 2 indicates heavy-tailedness of a distribution[88]), indicating the presence of infrequent yet strong positive connections (Fig. 3b). In contrast, the negative connections showed an opposite pattern, characterized by weak strength but with a considerable proportion in the entire network (40%).

Next, we examined the directionality of iEC with respect to two network measures: weighted degree distribution and intrinsic signal flow. In the analysis of weighted degree distribution, we calculated the ratio of connection polarity (*i.e.*, negative *vs.* positive) for both out- and in-degree ECs (**Supplementary Fig. 5a**). This revealed a discernible dominance of positive outdegree ratios within the sensory cortices, contrasted by a prominent presence of negative outdegree ratios in the heteromodal areas. More specifically, when we categorized them based on hierarchically ordered functional networks[85], the proportion of signed connectivity showed a similar trend with the macaque tract-tracing result (Fig. 3c): a disproportionately large amount of positive ECs from early sensory areas and a balanced presence of positive and negative ECs from heteromodal areas, which may represent the influence of FF and FB pathways, respectively[89].

To further explore the impact of this connection topology on signal propagation across the cortex, we employed a linear dynamical system analysis that examines ‘unconstrained signal flow’ from predefined seed areas[16] (Fig. 3d; see **Methods** ‘*5.2 Signal flow analysis*’). This analysis revealed that positive signals predominantly originate from hierarchically lower cortical areas, whereas negative signals are almost exclusively sent from the high-order to low-level regions. Moreover, each of unimodal and heteromodal areas showed strong positive signals within their module, suggesting highly specialized functional subsystems (Fig. 3e). In sum, our findings suggest that the iEC has the potential to recapitulate the principle of signal flows across areas of varying hierarchical levels (see **Supplementary Fig. 6** for reproducibility in the replication dataset).

2.2 Retrieving signal flow hierarchy from iEC

The iEC analyses conducted so far have provided converging evidence indicating distinct signatures of directed functional connectivity that reflect hierarchical organization, including *i)* a significant relationship between iEC patterns and FF/FB connectivity in the macaque brain (Fig. 2f), *ii)* a different proportion of positive/negative signaling along the sensory-association axis in the human brain (Figs. 3c and 3d), and *iii)* the observation that the majority of negative signal flows occurred in the heteromodal-to-unimodal pathways (Fig. 3e). These findings collectively motivated a systematic evaluation to assess whether iEC can provide any useful information to determine hierarchical levels of the cortical areas in the human brain.

To address this question, we employed an established modeling framework[84,90], originally designed to quantify the hierarchical levels of cortical areas and examined their presumed top-down and bottom-up connectivity topologies. Traditionally, this framework has been reserved for macaque studies due to the necessity of histological data (*e.g.*, SLN values), through which the feedforward and feedback properties of the connections could be inferred. However, as our findings (Fig. 4a) also provide insights into inferring the hierarchical levels of cortical areas, we used the group-level iEC matrix as a substitute for SLN to reconstruct a signal flow hierarchy map of the human brain using this framework (see **Methods** ‘*5.3 Hierarchy estimation*’).

The mapping of this signal flow hierarchy revealed a distinct and organized structure (Fig. 4b): primary sensory and motor areas occupy the lowest tiers, while paralimbic cortices, such as the anterior cingulate, insular, and parahippocampal regions, are positioned at the highest levels of cortical hierarchy. This pattern was partly comparable yet still distinct enough from a well-known functional gradient[15], a dimension-reduced topographic map of (undirected) FC representing a sensory-association axis[28] (Fig. 4c). Indeed, there was a significant spatial correlation between our EC-based hierarchy and the functional gradient map ($r = 0.34$, $p < 0.001$). Yet, the paralimbic regions exhibited higher values exclusively in the EC-derived hierarchy map. This emphasis on the paralimbic regions aligns with Mesulam's initial proposition[71], in which these areas have been conceptualized as a 'neural bridge' linking the neocortex and hypothalamus (which directly monitors the internal milieu) (Fig. 4d).

The validity of our EC-based hierarchy map was further supported by the *post-hoc* analysis involving cyto- and myelo-architecture (**Supplementary Fig. 7a**). For the cytoarchitecture, we used Campbell's atlas[91,92], a historical neuroanatomy resource for microscopic cellular observation. When the brain areas in this atlas were sorted based on our EC hierarchical values, the pattern closely matched a known hierarchy stream: primary sensory areas at the base, followed by unimodal and heteromodal association areas and ending with paralimbic areas at the top. A significant correlation with myeloarchitecture (by Nieuwenhuys' atlas depicting a cortical myelin level[12]) was also found ($r = 0.42$, $p < 0.001$), underscoring the relationship between the signal flow hierarchy and its anatomical substrates (myelin degree), which has been previously reported to reflect the structural hierarchy of the brain.[93].

Most importantly, our validation drew upon the seminal '*Structural Model*' theory[94,95], which posits that FF/FB connections depend on the laminar structure of the connected areas. According to this model, FB connections typically originate from areas with simpler laminar structures ('agranular' or 'dysgranular') and target areas with more elaborate laminar structures ('eulaminate' or 'koniocortex'), and *vice versa* for the FF connections (*i.e.*, more elaborate to simpler laminar targeting). Inspired by this theory, we tested our hierarchy map by examining its whole-brain profile across different cortical types (Fig. 4e). This analysis revealed a highly significant alignment (GLM $t = 5.14$, $p < 0.001$), with a progressive increase in hierarchy corresponding to decrease of granular layers (see **Supplementary Fig. 7b** for the result when measured based on the functional gradient).

Finally, we again performed the unconstrained signal flow mapping on iEC, yet this time with the cortical areas sorted out by Mesulam's cortical zones. This analysis revealed that the pattern we have previously hypothesized in terms of FF (*i.e.*, largely excitatory) and FB signaling (balanced excitatory and inhibitory influences) are well captured in our EC-based cortical hierarchy (Fig. 4f). Indeed, both primary sensory and unimodal association areas mostly emit positive signals, while the heteromodal regions show a balance between positive and negative signal flows, and this pattern even converts in the paralimbic region to the one with negative signals exclusively detected.

2.3. State-dependent reorganization of signal flow hierarchy

Although the hierarchy map we derived from resting state fMRI provides compelling evidence for biological validity, it is still derived from only a single specific brain state, which occurs without explicit environmental engagement. The next logical question was therefore if this hierarchical organization remains preserved (as a backbone of default functional dynamics) even when the brain transitions to other functional states, or if it is reorganized to optimize neuronal information processing in response to contextual changes (*i.e.*, state-dependent functional reconfiguration). To address this question, we analyzed two additional neuroimaging datasets, each representing a major (non-resting) brain state: one from fMRI scans conducted during movie watching (‘Forrest Gump’) and another during the experience of tonic pain induced by oral capsaicin delivery (see **Methods** ‘*1. Data acquisition*’). The former captures an externally focused state, where attention is directed towards visual and auditory stimuli (*i.e.*, primarily exteroceptive), while the latter represents a more internally focused state, where awareness is concentrated on sustained painful sensation within mouth (*i.e.*, more interoceptive). Both the group-level iEC matrix and signal flow hierarchy were constructed using the same procedure as in the previous analyses (see **Supplementary Fig. 8** for iEC results).

When directly correlating the spatial patterns of hierarchy maps across different states, we found that both movie-watching and tonic pain states exhibit trends similar to the resting state (Fig. 5a; $r = 0.46/0.64$, respectively; both $p < 0.001$), suggesting the stability of overall functional hierarchy across different brain states. Despite this globally shared pattern, each state also displayed its idiosyncratic hierarchical changes. To explore this within the framework of Mesulam’s cortical organization (Fig. 4d) — which uniquely stratifies cortical areas based on their role in processing the external environment *versus* the internal milieu — we assessed the hierarchical levels of four cortical zones: primary sensory, unimodal and heteromodal association, and paralimbic areas. Firstly, the signal flow hierarchy in the resting state, consistent with our previous analysis (Figs. 4e-g), demonstrated a monotonically increasing hierarchy across these cortical zones (Fig. 5b, orange).

Compared to this, however, during the movie-watching state (Fig. 5b, pale green), the primary sensory and unimodal association areas showed an elevated hierarchy, while the heteromodal association and paralimbic areas exhibited an opposite pattern, overall suggesting a signature of ‘flattened cortical hierarchy’. This is consistent with a recent finding reported in a naturalistic fMRI study[96]. This hierarchy change was explained by the subsequent signal flow analysis (Fig. 5c left), which demonstrated 1) an overall decrease of positive signals from the primary sensory areas, 2) another decrease of negative signals from paralimbic areas, and 3) an increase of negative signals in the unimodal association areas (*i.e.*, higher-order visual cortices), collectively resulting in less differentiated hierarchical levels throughout the whole brain (‘hierarchical flattening’). Notably, the latter observation, an increase of negative signals from the higher-order visual areas, was found to mostly target auditory regions, potentially suggesting a competing modulatory effect of shared attentional resources[97] and/or multisensory integration[98]. This state-dependent reorganization during movie-watching therefore suggests a shift in cognitive load towards externally oriented processes, as indicative of altered FF/FB signaling along sensory and attention pathways[99–101].

In contrast, the tonic pain condition led to a brain state with a steeper hierarchical gap between the paralimbic and non-paralimbic areas (Fig. 5b, pale purple). Again, the signal flow mapping provided a parsimonious account for this change, demonstrating a decreased negative signal emission from the heteromodal association areas (particularly from the angular gyrus; Fig. 5c right), which may cause their hierarchy levels to diminish (thus resulting in a larger disparity between the paralimbic and non-paralimbic areas). This also indicates a state-dependent hierarchical shift, but different from a movie-watching condition, the brain appears to focus on mostly top-down effects of interoceptive areas by rendering the negative signals to be emitted primarily from the paralimbic system. This may suggest the prioritization of an allostatic control to cope with a potential danger from sustained pain[102,103].

We finally note that there is also a state-general component across all three brain conditions: strong negative signal flows from 'paralimbic/heteromodal to unimodal' regions (especially from the cingulate and orbitofrontal areas; Fig. 5a), highlighting the importance of their state-invariant modulatory effect. In sum, these results suggest that while the global pattern of signal flow hierarchy may be relatively preserved across different states, the degree of hierarchy and its functional dynamics can be significantly adjusted to more efficiently respond to the given (either external or internal) environmental changes.

Discussion

Ever since Hubel and Wiesel's initial discovery in the visual cortex[104], functional hierarchy has been a central topic in systems neuroscience, serving as a primary basis to study the principle of neural information flow. While early work tended to focus on the sensory hierarchy[105,106], the notion of this hierarchical architecture has been more broadly expanded over the last two decades, recently emphasizing the significance of its whole-brain representation spanning from the sensorimotor to association areas[9,10,16,80,93,107,108]. In this study, we reconstructed a biologically grounded signal flow functional hierarchy of the human cerebral cortex in a fully data-driven manner, analyzing different brain states across multiple fMRI datasets. Given that the hierarchy is inherently organized by '*directed*' feedforward (FF) and feedback (FB) pathways[84,109], we employed macroscale effective connectivity, linearly combining the results of existing individual algorithms (iEC). This collective inference was demonstrated not only to boost the accuracy of directionality estimation but also to allow for the discovery of interesting relationships between signed (positive and negative) connections and histologically derived FF/FB pathways, providing a crucial hint to infer a hierarchical structure from in-vivo fMRI. Indeed, our iEC-based hierarchy revealed a strong alignment with a spatial distribution of hierarchy-indexed cyto- and myelo-architectonic features as well as the laminar proportion of granular cells across the brain, effectively recovering the 'sensorimotor-association-paralimbic' axis, as originally proposed in Mesulam's cortical zone[71]. Moreover, we found that this functional axis does not always adhere to a fixed hierarchy, but instead reorganizes dynamically according to brain states, potentially enhancing behavioral adaptability in response to rapidly changing environments. Our findings thus offer a novel avenue to quantitatively probe state-dependent neural information flows along the biologically validated signal flow hierarchy in both typical and atypical human brain conditions.

The idea behind how fMRI-based iEC enables the estimation of signal flow hierarchy was built upon multiple observations on our iEC profiles and their interpretation in the context of previous literature. Traditionally, the FB connections, for instance those observed between the cortex and thalamus, were primarily considered to exert a modulatory (often inhibitory) effect, refining bottom-up sensory information[110–115]. However, emerging evidence indicates a more active role of FB connections, not only as a modulator but also as a driver to increase the neural activity (excitatory)[116,117], especially for hierarchically proximate cortical areas[81–83]. In contrast to such mixed neurophysiological effects of FB, the characteristic of FF connections has been almost exclusively associated with excitatory effects on the targeted area (but see the recent perspectives[118,119]). For example, in the macaque brain, experimentally silencing V1 through cooling strongly suppresses neural activities across the series of hierarchically connected areas from V2 to V5/MT, highlighting a significant driving role of FF pathways[120–125].

Importantly, these distinct excitatory-inhibitory patterns between FF and FB connections also seem observable in our macroscale iEC profiles, assuming that positive iEC generally represents an excitatory effect whereas negative iEC relates more to an inhibitory effect. Parallel to this notion, when associating the sign of iEC and the patterns of supragranular labeled neurons (SLN), a histological metric to quantitatively determine the degree of FF/FB pathways in the macaque brain, we found a unique pattern of ‘*signed iEC asymmetry*’ gradient: FF connections, as determined by SLN, were characterized by a disproportionate ratio of positive iECs, whereas FB connections additionally exhibited a significant increase of negative iECs, resulting in a more balanced distribution of signed iECs. A similar asymmetry gradient was also observed in the human brain, where low-level sensory areas, known as key sources of FF signaling[1,90,121,126], exhibited a dominant proportion of positive iECs, whereas the higher-order association areas (major sources of FB signaling[127–132]) displayed progressively enhanced negative iECs in addition. These cross-species findings, together with the previously hypothesized role of FF/FB connections, collectively suggest that despite its macroscale nature derived from fMRI, iEC may contain biologically meaningful signals to infer the trace of FF/FB connections, which provides a testable ground to reconstruct the signal flow hierarchy *in vivo*.

Given this motivation, we indeed analyzed the iEC matrix in more depth to quantitatively reconstruct the signal flow hierarchy, inspired by the seminal macaque studies[84,90]. Specifically, we used a general linear model (GLM) to estimate a hierarchy difference between the two brain areas (*i.e.*, source and target) according to the following, very simple rule: if the source exerts dominantly positive (or negative) influences on the target, the former cortex ranks lower (higher) than the latter one in the hierarchical axis. However, when it comes to more complex networks such as the one analyzed in our study (*i.e.*, 360 nodes that generates $> 10^5$ connections), calculating the analytical solution of GLM that is 100% satisfactory in terms of correctly ranking all brain areas without any violation is not possible, because of their complicatedly intertwined EC relationships. Instead, what the GLM solution provides is the hierarchy setting with ‘the least tension’ across brain regions. That is, although the hierarchy level is overall properly assigned across the brain, there could still be some areas positioned at a relatively higher hierarchical level, yet they may emit (not only negative iECs but also) a large amount of positive ECs to other brain regions (*e.g.*, heteromodal areas in our map). It should be noted, therefore, that this hierarchy assignment is not simply a problem between the two brain nodes but is a collective result, for which one has to take into account all other relationships with the rest of the brain.

Despite such computational complexity, our iEC-based method revealed several biologically noteworthy findings in hierarchy mapping. Firstly, compared to the widely used connectome compression approach called ‘functional gradient’[15], which places the default mode network in the apex of the hierarchy, our iEC-based result puts more emphasis on the paralimbic regions to characterize a hierarchical stream of the human brain, which is in parallel to the original proposition of Mesulam[71]. This suggests that although many studies currently focus on the sensory-to-association axis, framing it as a major functional organization principle, the axis should also take the interoceptive cortical areas into consideration, treating them as yet another pivotal anchor. This finding highlights the importance of homeostatic and allostatic body regulations of the internal environment in goal-driven interactions with the external world. This is supported by our observation on the elevated paralimbic hierarchy (with flattened other areas’ hierarchy) during the tonic-pain condition (Fig. 5b), suggesting that the brain may inherently prioritizes the processing of interoceptive inputs over exteroceptive counterparts in certain contexts. Secondly, the validity of our hierarchy was also corroborated by histological architectonic maps[12,91,92], together with the cortical type analysis based on the ‘Structural Model of laminar connectivity’[11,95]. Notably, when we compared this hierarchy pattern to the one reconstructed based on only the positive iEC (thus assuming that their difference stems from the negative iECs), the paralimbic areas with a diminished laminar organization (*i.e.*, dysgranular and agranular cortices) exhibited the largest hierarchy changes (**Supplementary Fig. 9**) across the entire cortical zones, suggesting a significant contribution of negative iECs in precisely capturing the properties of hierarchically higher-order cortical regions, particularly for their potential FB modulation effects.

Most importantly, our findings underscore the significance of dynamic and flexible reconfiguration of the functional hierarchy based on given brain states. This phenomenon, termed ‘*state-dependent hierarchical reorganization*’, is critical for the adaptive functioning of the brain. Indeed, despite the largely static nature of its ‘anatomical’ hierarchy, the state-dependent shifting mechanism enables transiently reconfiguring a large-scale functional architecture of the brain, allowing it to effectively respond to moment-by-moment environmental and task-related changes, and thereby enhancing its overall viability. Indeed, the seminal paper by Felleman and Van Essen 1991[1] had already conjectured the possibility of this mechanism in the following sentences: *“Another possibility is that a hierarchy exists only in a loose sense, for instance, at the level of the different cerebral lobes, but not in any precisely definable manner for individual cortical areas.”*, (Providing an analogy with human societies) *“... Some organizations have an utterly rigid hierarchy, in which every individual knows precisely his or her place within a pecking order. Others are less well defined … may be inherently fluid and context dependent, in that one person ranks above another in one particular circumstance but below the other in another circumstance.”.* We believe that our discovery of the state-dependent reorganization offers novel insights into how the brain forms such a context-dependent functional hierarchy. The finding of flexibly elevated or flattened hierarchy in specific cortical regions in response to different environmental contexts exemplifies such a phenomenon. It will offer compelling evidence for the principles of functional brain adaptability, especially when it is combined with more neurobiologically grounded circuit mechanisms, such as neuromodulatory controls via cortico-subcortical loops[133,134].

Beyond the biological implications, our findings also offer methodological insights, especially for modeling studies in a large-scale network simulation of the human brain, a research field recently garnering great attention in computational and clinical neuroscience[135–139]. While previous work targeted to study the effects of 'local' biophysical parameters to simulate brain signals (*e.g.*, recurrent excitatory and inhibitory-to-excitatory connections)[138,140], recent evidence increasingly indicates that the 'global' properties of long-range connections could also be critical in shaping macroscale dynamics[141–143]. In parallel to this trend, our findings also highlight the role of heterogeneous connectional properties, such as the embedding of cortical hierarchy, directed signal flows, and their weighted signs, in simulating more biologically plausible functional dynamics. Indeed, our *post-hoc* analysis suggested that the 'negative' iEC, despite their substantially weak strength, is essential to boost the EC-to-FC recovery (**Supplementary Fig. 4b**), as well as to capture the cortical hierarchy in paralimbic regions (**Supplementary Fig. 9**). Amid ongoing debates regarding the role of macroscale inter-areal connections in shaping spatiotemporal brain activity patterns[144–146], our study highlights the necessity of accounting for heterogeneity in global connectivity structures, an aspect that has been largely overlooked in prior modeling research.

Effective connectivity, pioneered by Friston in 2003[147], has evolved to encompass concepts such as directed functional connectivity and information flow[50,96]. Despite its importance, the perception within the field regarding this methodology has been rather divergent. On the one hand, there has been appreciation for the development of many different algorithms for estimating directionality using technically advanced statistical methods[35,44,46–48,59]. On the other hand, the practical application of these algorithms has left a somewhat mixed impression. In particular, the overabundance of specialized algorithms designed to address specific issues has made it difficult to make a consensus in terms of how to navigate the array of options to find the most suitable algorithm for their research interests. The creation of a unified methodology, rather than yet another sophisticated algorithm, was therefore crucial for advancing the field. The effectiveness of our integrative and unified framework is demonstrated by its enhanced accuracy across various atlas resolutions and data types, including both human and macaque brain networks, and its reproducibility at both individual and group levels. Our methodology thus paves the way for a more streamlined and cohesive approach to effective connectivity mapping of the human brain.

Several limitations should be acknowledged. First, the algorithms used in our study do not encompass the entire spectrum of available EC methods, particularly in light of recent advancements such as deep learning models ranging from graph neural networks to transformers[148–153]. Nonetheless, our framework is not restricted to specific algorithms but is open to testing any other combination of mathematically distinct yet complementary methods, which could be a future research topic. Second, our integration process relied on a linear approach, with which we cannot capture more complex nonlinear relationships between input algorithms and outcomes. However, our simple linear method could preserve the topology of each connectivity matrix and requires only a few minutes of computational time, with the added benefit of straightforward interpretability. Third, we did not include subcortical structures (*e.g.*, thalamus and hippocampus) in our iEC framework, which may lead to some deficiency in reconstructing the whole-brain hierarchy map, especially considering that they often play a central role in creating structured neural activities across macroscale brain networks[134,154–157]. However, given that the signal-to-noise ratio of fMRI signals is generally low in these deep brain structures, when we examined the iEC profiles covering the whole brain, the pattern in the subcortical structures showed almost negligible EC magnitude in single algorithms compared to the neocortex, which made us preclude their involvement for the calculation of iEC. Analyzing higher gradient-field MRI data will be required to address this issue. Lastly, we did not account for local heterogeneity, such as the varying coupling values of excitatory and inhibitory populations within regional circuits, which is another crucial feature of the brain[93,158–160]. Future research could incorporate these two different scales of heterogeneity (local properties of cell populations *vs.* global connectional topology and information flow properties) and explore how these factors interact to shape spatiotemporal brain activity.

Methods

1. Data acquisition

Throughout this study, we analyzed human and non-human primate data for simulation and empirical iEC analyses. In this section, we first provide the data description and then the details of their image processing steps.

1.1 Macaque tract-tracing data

We have analyzed macaque tract-tracing data from Froudist-Walsh *et al.* (2021)[10], which provides a comprehensive overview of cortical connectivity through retrograde tracer injections. Specifically, the tracers injected into specific cortical targets were transported to neuron cell bodies across the brain, except the injection site. These neurons, termed labeled neurons (LNs), were quantified in source areas projecting to the target. To standardize connection strengths, we calculated the fraction of labeled neurons (FLN) by dividing the number of LNs in a source area by the total LNs, excluding the injection site. Additionally, we measured the supragranular labeled neurons (SLN), indicating the proportion of labeled neurons in 2–3 layers with respect to a total labeled neuron number in the source area. This ratio has been used to characterize the feedforward and feedback nature of the connections, based on the established observation that feedforward pathways predominantly originate from the supragranular layers, whereas feedback pathways primarily arise from the infragranular layers[1,84,161].

1.2 Macaque neuroimaging data and preprocessing

We also analyzed 3T resting-state fMRI data from 19 anesthetized macaques from PRIME-DE database (UC-Davis site)[77]. The fMRI was acquired using Siemens Skyra scanner with 4-channel clamshell coil, with the following parameters: 1.4-mm isotropic voxels, repetition time (TR) = 1600 ms, echo time (TE) =

24 ms, field of view (FOV) = 140mm. We employed a HCP-style preprocessing pipeline to process fMRI data[162], which included: anatomical structure reconstruction and segmentation, normalization to a standard brain template, correction for spatial and temporal distortions, and motion correction and resampling for surface and voxel data. Additional nuisance regression was applied to the fMRI data for denoising, which included: 12 motion-related regressors (motion parameters and derivatives thereof) and 5 principal components from white matter and ventricles and their derivatives (in total 32 regressors). The resulting signal was high pass filtered at 0.008Hz to remove noise induced by slow drift.

1.3 Human neuroimaging data and preprocessing

1.3.1 Demographics

To compare the functional hierarchy and signal flow across the hierarchy across different brain states, our study included three distinct human fMRI datasets: resting-state fMRI, movie-watching fMRI, and tonic-pain fMRI. For the resting-state dataset, we utilized the S1200 release from the Human Connectome Project (HCP)[163]. After excluding participants with excessive head motion, we analyzed data from 440 participants (mean age 28.8 years, 245 females). For the movie-watching dataset, we used the 'StudyForrest' dataset from Sengupta et al.[164], excluding two participants due to excessive head motion, resulting in a final sample of 13 participants (mean age 29.4 years, 6 females). Finally, for the tonic-pain dataset, we employed data from Lee et al.[165,166], which included 48 participants after excluding participants with excessive head motion (mean age 22.8 years, 21 females).

1.3.2. Human neuroimaging data and preprocessing

1. *HCP S1200 dataset*: MRI scans were conducted using a customized 3-T Siemens Connectom Skyra scanner equipped with a standard Siemens 32-channel RF receive head coil. T1-weighted structural images were acquired with 0.7-mm isotropic voxels, a TR of 2400 ms, an TE of 2.14 ms, and an FOV of 224×224 mm. T2-weighted functional images were obtained with 2.0-mm isotropic voxels, a TR of 720 ms, a TE of 33.1 ms, and an FOV of 208×180 mm.
2. *StudyForrest dataset*: In this dataset, participants engaged in a naturalistic audio-visual task by watching and listening to the movie *Forrest Gump*. The MRI data were acquired using a 3-Tesla Philips Achieva dStream scanner with a 32-channel head coil. T1-weighted images were captured with 0.67-mm isotropic voxels, a TR of 2500 ms, a TE of 5.7 ms, and an FOV of 191.8×256×256 mm. T2-weighted functional images were acquired with 1.4×1.4×1.5 mm isotropic voxels, a TR of 2000 ms, a TE of 30 ms, and an FOV of 240 mm.
3. *Tonic-pain dataset*: To induce tonic pain, we delivered the capsaicin-rich hot sauce onto the participants’ tongues, and participants continuously rated their pain during the run. The fMRI scan duration was 20 minutes to fully cover the entire period of sustained pain from its initiation to the complete remission. The MRI data were acquired using a 3-T Siemens Prisma scanner with a 64-channel head coil at Sungkyunkwan University. T1-weighted structural images were acquired with 0.7-mm isotropic voxels, a TR of 2400 ms, a TE of 2.34 ms, and an FOV of 224×224 mm. T2-

weighted functional images were acquired with 2.7×2.7×2.7 mm isotropic voxels, a TR of 460 ms, a TE of 27.2 ms, and an FOV of 220 mm.

The preprocessing steps of fMRI data are thoroughly documented in the respective original manuscript for each dataset. In brief, we aimed to adhere as closely as possible to the HCP pipeline across all datasets to maintain consistency. This pipeline includes several critical steps: correcting for spatial and gradient distortions, compensating for head motion, normalizing signal intensity, removing bias fields, aligning data with T1-weighted structural images, and conforming to the 2-mm standard Montreal Neurological Institute space. Furthermore, head motion artifacts and structured noise were mitigated using a combination of independent component analysis and FMRIB's ICA-based X-noiseifier (ICA + FIX)[167]. However, it is important to note that this specific classifier is not universally applicable to other neuroimaging data obtained with varying MRI specifications and acquisition protocols. Therefore, for the movie-watching and tonic pain datasets, we opted to employ ICA-AROMA[168], which operates on a conceptually similar basis to ICA + FIX but is designed for more general datasets. Indeed, the two denoising approaches are only different in the way the noise components are classified, allowing us a close comparison of fMRI data across different states. Additionally, we regressed out mean CSF and WM signals from the denoised data to further exclude non-neuronal signals from our final analysis. The resulting signal was high-pass filtered at 0.008Hz to remove noise induced by slow drift. In our parcel-level analysis, we obtained the average time series for every vertex within each region defined by the Schaefer (bilaterally 100 parcels) or MMP (bilaterally 360 parcels) atlas, resulting in the final parcel-level BOLD time series.

1.3.3 Diffusion MRI data

To construct a high-quality SC matrix, we employed diffusion-weighted imaging (DWI) data of 86 young-adult subjects from the Q3 release of the HCP database[169], to be independent (thus unbiased) from our main resting-state fMRI analysis. The HCP DWI scans were acquired using a customized 3-T Siemens Connectom Skyra scanner with a standard Siemens 32-channel RF receive head coil, with the following parameters: 2.0-mm isotropic voxels, TR = 5520 ms, TE = 89.5 ms, FOV = 208×180 mm (The detailed preprocessing steps are thoroughly documented in the original manuscript[170]).

To first estimate the fiber orientation distributions[171–173] from the preprocessed DWI data, we first employed a multi-shell, multi-tissue constrained spherical deconvolution process using MRtrix3. We then used a deterministic tractography algorithm to construct the tractogram from the estimated fibers[174], employing the algorithm's default settings with modifications only to the maximum length (250 mm) and the number of streamlines (5 million). To enhance accuracy in the tractogram, we applied a filtering method[175], which minimizes spurious fiber tracking. SC matrices were then generated by counting the stream lines between brain regions based on two cortical parcellations: Schaefer-100 and MMP-360. As a final step in constructing a group-level SC matrix, we averaged the individual SC matrices and applied a threshold to retain the top 15% of connections for a balanced trade-off between sensitivity and specificity[176].

1.3.4 synthetic directed structural connectivity

Our synthetic directed network generation began with the group-level SC derived from the DWI data above. We introduced directionality into this matrix using the '*randmio_dir_connected.m*' from the Brain Connectivity Toolbox[177]. This function randomly rewires a subset of edges (total 30% of edges are rewired at each network generation) within the original SC matrix, with the constraint of preserving the network's original degree distribution. By inducing directionality in this manner, we maintained the overall integrity and architecture of the empirical SC, resulting in a biologically plausible synthetic directed SC.

2. Effective connectivity algorithms

Over the past two decades, the proliferation of diverse EC algorithms has underscored the field's growth but has also introduced challenges in achieving consensus and reproducibility due to varying methodological approaches. To address these challenges, here we developed the iEC method. One crucial aspect of its development was the characterization of existing algorithms. To this end, we created a comprehensive taxonomy of EC algorithms by categorizing them into two primary groups: ‘graphical model’ and ‘dynamical system’. These categories fundamentally differ in their approaches to estimating directed influence. The graphical model category, particularly Bayesian network analysis, utilizes concepts from Bayesian probability theory (*e.g.*, d-separation and conditional independence) to infer the presence and directionality of connections. In contrast, the dynamical system category employs linear or nonlinear dynamics to model data and infer the connectivity matrix. Further, we subdivided the graphical model category into algorithms that can infer cyclic connections and those that cannot (acyclic), while the dynamical systems category was divided into lag-based models and dynamic causal models. Following this, we implemented a screening process to select representative EC algorithms within each category, guided by specific selection criteria:

1) *Cyclic connections*: The algorithm must possess the ability to infer cyclic (*i.e.*, recurrent) connections within the network, as the brain comprises a dense network of reciprocal connections (*e.g.*, 26 to 42% of observed connections are reciprocal in macaque brain[84,178]).

2) *Scalability to high-resolution networks*: The algorithm should be able to compute high-resolution networks, given that the human brain is known to comprise at least 100 functionally distinct brain areas[60,179], and the widely used brain atlases for human consist of more than 300 nodes[61,180].

3) *Mathematical uniqueness*: To avoid redundancy, we selected one algorithm per category. If two algorithms share similar mathematical underpinnings, their EC estimates are likely to yield similar outputs, thus an algorithm with either lower performance or higher computational cost was excluded from the list of candidate algorithms.

In the Bayes network category, we removed all algorithms that cannot infer cyclic connections (*e.g.*, Patels’ tau method), and within ‘cyclic’ category, we then selected one algorithm that takes less computation time for high resolution networks (*i.e.*, scalability) to choose a representative algorithm of this category resulting in the following algorithm:

1) **FASK** *(Fast Adjacency Skewness)*[41]: This method was chosen from the Bayesian net approaches. Its suitability arises from the capability to infer cyclic connections and amenability to high-resolution network analyses. For instance, regarding the BOLD signals parcellated based on MMP-360, it takes on average four minutes to estimate effective connectivity from a subject.

Within the lag-based category, the major algorithms were vector autoregressive models, transfer entropy, and Granger causality. These algorithms are capable of detecting cyclic connections. However, it has been demonstrated that Granger causality and transfer entropy are theoretically equivalent for Gaussian variables[181], with the key distinction being that transfer entropy can detect nonlinear relationships and is applicable to non-Gaussian variables[182]. Given recent findings suggesting that macroscopic brain signals, such as fMRI, are best modelled with a linear method[183] and follow Gaussian[184], we excluded transfer entropy. Furthermore, vector autoregressive models have been shown to outperform deep learning-based nonlinear models[185] while also being computationally efficient. As a result, we selected the following algorithm:

2) **VAR** *(Vector Autoregression)*[186]: This was selected for the Lag-based category. The algorithm is well-suited for our iEC framework due to its ability to detect cyclic connections, infer both negative and positive connections, and its exceptionally fast computation time (*e.g.*, estimating effective connectivity from a subject using MMP-360 parcellation in just a few seconds), and the recent reports highlighting its superior performance in modeling macroscale brain dynamics, such as those observed in fMRI data[185].

Lastly, within the dynamic causal model category, we identified only one viable candidate due to the scalability requirements. Many algorithms in this category are computationally prohibitive[45,187], but our selected algorithm demonstrated comparable performance to more computationally intensive models[36]. As a result, we chose the following algorithm:

3) **rDCM** *(regression Dynamical Causal Modeling)*[36]: This algorithm was opted for Dynamic Causal Modeling (DCM) analysis, as it is the only one method that can be applied to the high-resolution networks among DCM algorithms. For example, spectral DCM, which yields results comparable to rDCM[36], requires approximately 200 minutes per iteration for a graph with 36 nodes, with convergence typically achieved within 64 to 128 iterations.

The selected algorithms, with the exception of rDCM, include free parameters. At each stage of the analysis, we determined the optimal values of these parameters using the same metrics employed for the validation of the EC algorithms and found that their variance was minimal. Therefore, for each analysis stage—simulation, macaque fMRI, and human fMRI—we randomly selected 10 subjects to obtain the optimal parameters and subsequently used the mean of these values for the corresponding analysis stage. In the next sections, we explain the details of these selected algorithms. For clarity, we first define the mathematical notation used: lowercase letters (*e.g.*, x) represent nodes, uppercase bold letters (*e.g.*, **X**) denote matrices, and lowercase bold letters (*e.g.*, **v**) represent vectors.

2.1 FASK

The FASK infers an effective connectivity matrix through the following procedure. First, it constructs an adjacency matrix, which serves as a skeleton with no directionality. Next, the algorithm tests each edge in the adjacency matrix for the presence of a 2-cycle (*i.e.*, recurrent connectivity). If an edge is not a 2-cycle, the algorithm applies the Left-Right orientation rule to determine its directionality. Specifically, 2-cycle detection is performed by testing whether the differences between $corr(x, y)$ and $corr(x, y|x > 0)$, as well as $corr(x, y)$ and $corr(x, y|y > 0)$, are significantly non-zero. If this condition is met, the recurrent edges are added to the output graph . For the Left-Right orientation rule, the algorithm orients the edge as $x \rightarrow y$ in (*i.e.*, EC matrix), if:

$$\frac{E\left[xy\right| x > 0]}{E\left[x^2\right| x > 0\,]E[\,y^2|x > 0]} - \frac{E\left[xy\right| y > 0]}{E\left[x^2\right| y > 0\,]E[\,y^2|y > 0]} > 0$$

Otherwise, the edge is oriented as $y \rightarrow x$. The FASK algorithm inherently infers only the presence of connections, not their strength. Therefore, we employed a subsampling method[41,188], wherein we randomly sampled half of the BOLD signal using the '*datasample.m*' method from MATLAB, estimated EC from the subsampled signal, obtained 100 different estimates, and calculated their mean to produce the final EC matrix with continuous values ranging from 0 to 1. FASK utilizes three parameters: a p-value for pruning edges in the construction of the adjacency matrix (*i.e.*, the cut-off value for the conditional independence test), an orientation parameter used for testing correlation differences in the 2-cycle detection step, and a threshold value to remove nonsignificant edges after subsampling. We implemented FASK using the 'causal-cmd' method, which is available online (https://bd2kccd.github.io/docs/causal-cmd/). The further details of the FASK algorithm and its underlying principles can be found in the original article[41].

2.2 VAR

The VAR systematically describes the linear relationship across multiple interdependent time series. In the model, the multivariate time series is expressed as a linear combination of its past values, with the relationship defined by lag-order p. In fMRI analysis, where the temporal resolution is relatively slow, the best lag-order is typically 1 (see the reference[185] for a detailed analysis of the impact of lag-order on fMRI model fitting), which simplifies the model to:

$$\backslash\text{varvec}X_t = \backslash\text{varvec}A\backslash\text{varvec}X_{t-1} + \zeta_t$$

where $\backslash\text{varvec}X_t$ is the multivariate time series at time t, $\backslash\text{varvec}A$ is the matrix of regression coefficients at lag 1 (*i.e.*, the EC matrix), and ζ is the noise term. The $\backslash\text{varvec}A$ matrix is estimated using ordinary least squares with L2 regularization using a free parameter λ to enhance the model's robustness and prevent overfitting.

2.3 rDCM

The rDCM, unlike VAR, models the underlying generative process of the data. While VAR phenomenologically predicts future values of multivariate variables using vector regression, rDCM assumes that the data is generated by an underlying dynamical system, either linear or nonlinear, and fits the system's parameters to the observed data. Specifically, rDCM models the BOLD signal using a linear dynamical system, which is described as follows:

$$\frac{d\varvec{x}}{dt} = \varvec{A}\varvec{x} + \varvec{C}\varvec{u}$$

In this equation, $\varvec{x}$ denotes the activity of brain regions, $\varvec{A}$ is the effective connectivity matrix, $\varvec{C}$ is the input matrix, and $\varvec{u}$ is the external input to the system. The innovation of rDCM lies in its technique of converting time-domain signals into the frequency domain, thereby reducing the system's complexity, and enabling the use of multiple linear regression for a rapid inference[36]. rDCM employs the concept of variational free energy, which balances the reconstruction accuracy against model complexity, thus inherently guarding against overfitting.

It should be noted that in the original formulation, rDCM models the BOLD signal using a fixed linear hemodynamic response function before inferring the EC from underlying neural activity. In our study, given that each of the selected algorithms operates on a different level of brain signals, we removed this part from rDCM for consistency of the analysis (by editing '*tapas_rdcm_filter.m*'). Code is available online https://github.com/translationalneuromodeling/tapas/tree/master/rDCM

2.4 Integrated EC framework

We applied a linear combination approach to construct the integrated EC from individual EC estimations. To do this, individual EC results were weighted by optimal coefficients (*i.e.,* β values), which were determined through a Bayesian optimization to maximize the following objective function:

$$\beta^* = argmax_{\beta}\, \rho\left(iEC, T\right)$$

$$iEC = \frac{1}{N}\sum{}_n^N \beta_n EC_n$$

where, ρ is the correlation between the iEC and target matrix T. At each analytical level, we employed a distinct target matrix T to optimize beta values: 1) At the simulation level, the target was the synthetic directed SCs; 2) At the macaque level, it was the ground-truth FLN matrix, 3) For the human level, where the ground-truth does not exist, the correlation was measured between the empirical FC and simulated FC derived from the Hopf model with the identified iEC as the underlying long-range connectivity backbone (explained in the next section). Specifically, we utilized the '*bayesopt.m*' function from MATLAB to implement Bayesian optimization, which models the objective function probabilistically and iteratively selects the most promising variables to evaluate based on a trade-off between exploration and exploitation (see ref.[75] for more details).

For the iEC construction, participants (both macaques and humans) were divided into 'discovery' and 'replication' groups, with the exception of the movie-watching dataset, which was not divided due to its small sample size. Specifically, we first optimized the β values for individual algorithms using data from the discovery group. These values were then applied to the independent replication group and vice versa to construct iEC (see **Supplementary Fig. 6** for details). For the macaque fMRI, the discovery group consisted of a randomly selected subset of 9 macaques, while the replication group comprised the remaining 10 macaques. For human fMRI, participants were split evenly, with 220 individuals assigned to each group (discovery and replication) for resting-state fMRI data, and 24 participants in each group for tonic-pain fMRI data.

3. Validation of EC algorithms

We conducted a thorough validation of the selected EC algorithms using a three-step approach: i) simulating whole-brain activity with synthetic directed SCs, ii) analyzing empirical data from non-human primate brain networks, and iii) examining human brain networks. This process aimed to rigorously test the efficacy of the iEC framework. In the first step, we used directed SCs and the Hopf model to simulate BOLD signals with biologically plausible long-range connectivity, measuring performance by comparing the inferred ECs to the ground truth. In the second step, we employed macaque resting-state fMRI to infer ECs and compared them against the FLNs, a gold standard for macaque brain connectivity. In the final step, we inferred ECs from human resting-state fMRI and used them in the Hopf model to simulate BOLD signals, and measured the performance by correlating the simulated FC against empirical FC. In both the first and final steps, the Hopf model was integral for simulating whole-brain dynamics, and below, we explain the mathematical details of the Hopf model.

3.1 Hopf whole-brain model

In the first and last step of our three-step validation approach, we simulated whole-brain BOLD signals using the Hopf model. This model combines local dynamics, described by the Landau-Stuart oscillator, with global dynamics shaped by a connectivity matrix. Despite its simplicity, the Hopf model has been widely used to simulate whole-brain dynamics and has been shown to capture numerous neurobiologically significant phenomena[96,189,190] (for more details, see the original paper[76]). In brief, the Hopf model is governed by the following set of coupled differential equations:

$$\frac{dx_i}{dt} = [a_i - {x_i}^2 - {y_i}^2]x_i - \omega\,_i y_i + G\sum{}_j C_{ij}(x_i - x_j) + \epsilon\eta\,_i\,(t)$$

$$\frac{dy_i}{dt} = [a_i - {x_i}^2 - {y_i}^2]y_i - \omega\,_i x_i + G\sum{}_j C_{ij}(y_i - y_j) + \epsilon\eta\,_i\,(t)$$

Where $x_i$and y_i are components governing the local dynamics, a_i is a bifurcation parameter, ω_i is an intrinsic frequency of each node, G is a global scaling parameter, C_{ij} is a connectivity matrix, $\eta_i(t)$ represents additive Gaussian noise, scaled by ϵ. Following previous work[76], the value of bifurcation parameter a was set to be -0.01 for all regions, and the intrinsic frequency ω_i of each node was empirically estimated based on the averaged peak frequency of the BOLD signals associated with each brain region. In the first simulation step, synthetic directed SCs were used as C_{ij} to simulate BOLD signals, from which ECs were inferred and subsequently correlated with the ground-truth SCs. In the fMRI validation step, ECs derived from fMRI were used as C_{ij} to simulate BOLD signals, which were then correlated with the empirical BOLD to assess performance.

4. Neuroanatomical data

4.1 Cortical types

Von Economo and Koskinas were the first to identify cortical types in the human cortex, recognizing them through the consistent variations observed in the layers across different regions[191]. In our study, we adapted cortical types based on a recent re-evaluation of VonEconomo's micrographs[11]. Classification of cortical types were based on several criteria, including the development of layer IV, the prominence (marked by denser cellularity and larger neurons) of either deep (layers V–VI) or superficial (layers II–III), the definition of sublayers (such as IIIa and IIIb), the distinctness of boundaries between layers, and the presence of large pyramidal neurons in superficial layers. These cortical types reflect a spectrum of laminar complexity, from the highly elaborate koniocortical areas and the six distinct layers in eulaminate III-I to the ambiguous differentiation in dysgranular and the complete lack of layering in agranular regions. To identify the cortical types for each parcel in the MMP-360 atlas, we used the Brodmann cortical atlas along with data provided by García-Cabezas (2020[11]), which classified the cortical type of each Brodmann area. Specifically, we first assigned cortical type information to the parcels in the Brodmann atlas, and then upsampled this annotated atlas to align with the MMP-360 atlas. Additionally, we applied a general linear model to examine the linear relationship between cortical types (an ordinal variable) and signal flow hierarchy levels (a continuous variable). This analysis was conducted using MATLAB's 'fitglm.m' function.

4.2 Cytoarchitecture and myeloarchitecture

The 1905 edition of the Campbell atlas[92] delineates 17 distinct cortical regions, closely mirroring the cortical organization proposed by Mesulam[71]. The arealization is primarily based on histological features, such as cyto- and myelo-architectures, where regional boundaries are determined by variations in laminar arrangement and number of fibers and neurons. Each region is given a name reflective of its function and/or geographical location, examples being the visual-sensory area and the temporal area. We used data from ref[91] for the cortical projection of the Campbell atlas in our analysis. For the myeloarchitecture data, we employed a 3D projection of the Vogt-Vogt legacy data, which is founded on a comprehensive meta-analysis and corroborated by ground-truth histological data. Detailed protocols on the myelin data projection in cortical surface can be found in the original paper[12].

4.3 Mesulam’s cortical zone

In his seminal work[71], M. Mesulam introduced functional subtypes, or cortical zones, of the human cortex, building on comparative homology with macaque monkeys. The cortical zones— primary sensory-motor, unimodal and heteromodal association, paralimbic, limbic and—had been well established in macaques through detailed anatomical, physiological, and behavioral studies. Mesulam inferred the human equivalents of these zones by utilizing cytoarchitectonics, electrophysiological recordings, functional imaging, and the behavioral effects of focal lesions. In his ‘human-cortical-zone’ atlas, he annotated all areas of the Brodmann atlas. We used this annotated Brodmann atlas to create a cortical zone map of the human brain, which we then upsampled to align with the MMP-360 atlas. Additionally, we developed MMP-27 modules to more effectively capture the signal flow across cortical zones by subdividing the existing MMP-22 modules, while making minimal alterations to the original boundaries. Specifically, new modules were introduced whenever cortical zones extended beyond the existing boundaries, resulting in the formation of 27 distinct modules.

5. Network analysis

Below, we describe three methods that we used to profile the network characteristics of the whole-brain EC, including connectome profiles, signal flows, and the functional hierarchy estimation of the cerebral cortex.

5.1 Degree and positive/negative ratio calculation

For the connectome profile, we measured both the weighted in-degree and out-degree of ECs across the whole brain’s network. This process involved calculating the number of incoming and outgoing connections for each node, providing overarching connection architectures across different brain regions. Given an EC matrix, with columns representing source nodes and rows representing target nodes, the weighted degree for a given node i was calculated using the formula:

$$InDegree\left(i\right)=\sum\ _{i=1}^{N}EC_{ij}\vee$$

Similarly, the outdegree for node i was determined by:

$$OutDegree\left(i\right)=\sum\ _{j=1}^{N}EC_{ij}\vee$$

After establishing in- and out-degrees, we computed the ratio of positive to negative connections for both. This involved categorizing each connection as either positive or negative based on its sign and then calculating the ratios as follows:

$$PositiveRatio_{InDegree}\left(i\right)=\frac{\sum\ _{i=1}^{N}I(EC_{ij}>0)}{\mathrm{N}}$$

$$NegativeRatio_{InDegree}\left(i\right) = \frac{\sum_{i=1}^{N} I(EC_{ij} < 0)}{N}$$

where I is an indicator function that yields 1 if the connection meets the given condition. The out-degree ratios were determined using a similar approach, referencing the out-degree equation mentioned above. For the statistical comparison of the degree and edge strength distributions between the target matrix (*e.g.*, synthetic directed SC in the simulation analysis) and the inferred ECs, we utilized Pearson's correlation coefficient, implemented via the 'corr.m' function in MATLAB. All reported statistical values were FDR-corrected to account for multiple comparisons.

5.2 Signal flow analysis

In addition to a network profiling approach, we also examined the signal propagation throughout the cortex using a linear dynamical system analysis, simulating unconstrained signal propagation across the connectivity matrix[16]. First, the EC matrix was normalized to enhance the system's stability by adjusting its eigenvalue spectrum according to the following equation:

$$EC = \frac{EC}{\lambda}$$

Here, λ is the largest eigenvalue of the EC matrix, $c = 1$ to ensure system stability, and I denotes the identity matrix of size N×N, which was the same as the number of parcels in the brain atlases (*e.g.*, 360 for MMP atlas). We then tracked the temporal evolution of this activity as it propagates through the network pathways, governed by the differential equation $\dot{\varvec x} = \varvec E\varvec C \times \varvec x\left(t\right)$. This approach effectively simulates the unconstrained signal flow across the network as dictated by the EC matrix. To simplify the visualization of these directed communications among 360 nodes without loss of generality, we conducted this analysis within the framework of the 22 (or 27) modules in MMP, where cortical areas are grouped based on both anatomical and functional features and arranged in a hierarchical manner[61].

In the state-dependent analysis, we quantified the change in signal flow for each module by calculating the difference in outdegree between conditions, separately for negative and positive signal flows. To evaluate statistical significance, the Δ values (*e.g.*, positive outdegree difference between movie-watching and resting states) were standardized using z-scores. Modules exhibiting statistically significant changes in signal flow were identified by applying z-score thresholds corresponding to the one-tailed (α = 0.05) and two-tailed (α = 0.025) significance levels to detect substantial deviations from the mean.

5.3 Hierarchy estimation

Finally, to estimate the cortical hierarchy level based on the iEC matrix, we followed an established model from macaque studies[84]. This model draws upon the observation that the proportion of projections from the supragranular layers in the source area (SLN) measures a hierarchical distance between the source and target areas[1,90]. In our analysis, based on a series of findings implicating the potential relationship between the signed iEC and FF/FB pathways, we substituted the SLN matrix with iEC matrix. Then the hierarchical values were inferred using a following general linear model:

$$g\left(E[EC_{ij}]\right) = \beta_i - \beta_j$$

Here, β_i is the hierarchical level of area i and g is a function that relates an expected EC to the hierarchical distance between areas i and j. Extending this to the full EC matrix, we express the model as:

$$g\left(E[Y]\right) = X\beta$$

In this formulation, Y is a vector of EC values, β is a vector containing the estimated hierarchical levels, and X is an incidence matrix (a matrix that represents which projections are connected to which brain areas) constructed from the EC, with dimensions $p \times n$, where p is the number of projections and n is the number of areas. In our study, we assume the link function, g, to be the identity function, and solve the equation using least squares, which is equivalent to the approach of Barone et al. (2000)[90]. Additionally, in our study, we thresholded the EC matrix by retaining the top 15% proportion of the strongest absolute weights to obtain a balanced trade-off between sensitivity and specificity[176]. The general trend of signal flow hierarchy does not vary along the threshold values (see **Supplementary Fig. 10**).

References

1. Felleman, D. J. & Van Essen, D. C. Distributed hierarchical processing in the primate cerebral cortex. Cereb. Cortex 1, 1–47 (1991).
2. Hilgetag, C.-C., O'Neill, M. A. & Young, M. P. Indeterminate Organization of the Visual System. Science (1996) doi:10.1126/science.271.5250.776.
3. Hilgetag, C., O'Neill, M. A. & Young, M. P. Hierarchical organization of macaque and cat cortical sensory systems explored with a novel network processor. Philos. Trans. R. Soc. Lond. B Biol. Sci. (2000) doi:10.1098/rstb.2000.0550.
4. Tong, F. Primary visual cortex and visual awareness. Nat. Rev. Neurosci. 4, 219–229 (2003).
5. Adams, R. A., Shipp, S. & Friston, K. J. Predictions not commands: active inference in the motor system. Brain Struct. Funct. 218, 611–643 (2013).
6. Kravitz, D. J., Saleem, K. S., Baker, C. I., Ungerleider, L. G. & Mishkin, M. The ventral visual pathway: an expanded neural framework for the processing of object quality. Trends Cogn. Sci. 17, 26–49 (2013).
7. Bastos, A. M. *et al.* Visual areas exert feedforward and feedback influences through distinct frequency channels. Neuron 85, 390–401 (2015).

8. Chanes, L. & Barrett, L. F. Redefining the Role of Limbic Areas in Cortical Processing. Trends Cogn. Sci. 20, 96–106 (2016).
9. Huntenburg, J. M., Bazin, P.-L. & Margulies, D. S. Large-Scale Gradients in Human Cortical Organization. Trends Cogn. Sci. 22, 21–31 (2018).
10. Froudist-Walsh, S. *et al.* A dopamine gradient controls access to distributed working memory in the large-scale monkey cortex. Neuron 109, 3500–3520.e13 (2021).
11. García-Cabezas, M. Á., Hacker, J. L. & Zikopoulos, B. A Protocol for Cortical Type Analysis of the Human Neocortex Applied on Histological Samples, the Atlas of Von Economo and Koskinas, and Magnetic Resonance Imaging. Front. Neuroanat. 14, 576015 (2020).
12. Foit, N. A. *et al.* A whole-brain 3D myeloarchitectonic atlas: Mapping the Vogt-Vogt legacy to the cortical surface. Neuroimage 263, 119617 (2022).
13. Markov, N. T. *et al.* A weighted and directed interareal connectivity matrix for macaque cerebral cortex. Cereb. Cortex 24, 17–36 (2014).
14. Markov, N. T. *et al.* Cortical high-density counterstream architectures. Science 342, 1238406 (2013).
15. Margulies, D. S. *et al.* Situating the default-mode network along a principal gradient of macroscale cortical organization. *Proc. Natl. Acad. Sci. U. S. A.* 113, 12574–12579 (2016).
16. Parkes, L. *et al.* Asymmetric signaling across the hierarchy of cytoarchitecture within the human connectome. Sci Adv 8, eadd2185 (2022).
17. Taylor, P., Hobbs, J. N., Burroni, J. & Siegelmann, H. T. The global landscape of cognition: hierarchical aggregation as an organizational principle of human cortical networks and functions. Sci. Rep. 5, 18112 (2015).
18. Mesulam, M. M. From sensation to cognition. Brain 121 (Pt 6), 1013–1052 (1998).
19. Katsumi, Y., Theriault, J. E., Quigley, K. S. & Barrett, L. F. Allostasis as a core feature of hierarchical gradients in the human brain. Netw Neurosci 6, 1010–1031 (2022).
20. Samara, A., Eilbott, J., Margulies, D. S., Xu, T. & Vanderwal, T. Cortical gradients during naturalistic processing are hierarchical and modality-specific. Neuroimage 271, 120023 (2023).
21. Dong, H.-M., Margulies, D. S., Zuo, X.-N. & Holmes, A. J. Shifting gradients of macroscale cortical organization mark the transition from childhood to adolescence. *Proc. Natl. Acad. Sci. U. S. A.* 118, (2021).
22. Tong, C. *et al.* Multimodal analysis demonstrating the shaping of functional gradients in the marmoset brain. Nat. Commun. 13, 6584 (2022).
23. Zhang, H. *et al.* Cortical connectivity gradients and local timescales during cognitive states are modulated by cognitive loads. Brain Struct. Funct. 227, 2701–2712 (2022).
24. Saadon-Grosman, N., Arzy, S. & Loewenstein, Y. Hierarchical cortical gradients in somatosensory processing. Neuroimage 222, 117257 (2020).
25. Wang, X., Margulies, D. S., Smallwood, J. & Jefferies, E. A gradient from long-term memory to novel cognition: Transitions through default mode and executive cortex. Neuroimage 220, 117074 (2020).

26. Murphy, C. *et al.* Modes of operation: A topographic neural gradient supporting stimulus dependent and independent cognition. Neuroimage 186, 487–496 (2019).
27. Song, H., Shim, W. M. & Rosenberg, M. D. Large-scale neural dynamics in a shared low-dimensional state space reflect cognitive and attentional dynamics. *Elife* 12, (2023).
28. Sydnor, V. J. *et al.* Intrinsic activity development unfolds along a sensorimotor-association cortical axis in youth. Nat. Neurosci. 26, 638–649 (2023).
29. Sydnor, V. J. *et al.* Neurodevelopment of the association cortices: Patterns, mechanisms, and implications for psychopathology. Neuron 109, 2820–2846 (2021).
30. Dong, D. *et al.* Compressed sensorimotor-to-transmodal hierarchical organization in schizophrenia. Psychol. Med. 53, 771–784 (2023).
31. Hong, S.-J. *et al.* Atypical functional connectome hierarchy in autism. Nat. Commun. 10, 1022 (2019).
32. Xia, M. *et al.* Connectome gradient dysfunction in major depression and its association with gene expression profiles and treatment outcomes. Mol. Psychiatry 27, 1384–1393 (2022).
33. Caciagli, L. *et al.* Disorganization of language and working memory systems in frontal versus temporal lobe epilepsy. Brain 146, 935–953 (2023).
34. Royer, J. *et al.* Cortical microstructural gradients capture memory network reorganization in temporal lobe epilepsy. Brain 146, 3923–3937 (2023).
35. Andrews, B., Ramsey, J., Sanchez-Romero, R., Camchong, J. & Kummerfeld, E. Fast scalable and accurate discovery of DAGs using the best order score search and grow-shrink trees. Adv. Neural Inf. Process. Syst. abs/2310.17679, (2023).
36. Frässle, S. *et al.* Regression DCM for fMRI. Neuroimage 155, 406–421 (2017).
37. Duggento, A. *et al.* Multivariate Granger causality unveils directed parietal to prefrontal cortex connectivity during task-free MRI. Sci. Rep. 8, 5571 (2018).
38. Reid, A. T. *et al.* Advancing functional connectivity research from association to causation. Nat. Neurosci. 22, 1751–1760 (2019).
39. Mumford, J. A. & Ramsey, J. D. Bayesian networks for fMRI: a primer. Neuroimage 86, 573–582 (2014).
40. Ramsey, J. D., Sanchez-Romero, R. & Glymour, C. Non-Gaussian methods and high-pass filters in the estimation of effective connections. Neuroimage 84, 986–1006 (2014).
41. Sanchez-Romero, R. *et al.* Estimating feedforward and feedback effective connections from fMRI time series: Assessments of statistical methods. Netw Neurosci 3, 274–306 (2019).
42. Vicente, R., Wibral, M., Lindner, M. & Pipa, G. Transfer entropy–a model-free measure of effective connectivity for the neurosciences. J. Comput. Neurosci. 30, 45–67 (2011).
43. Seth, A. K., Barrett, A. B. & Barnett, L. Granger causality analysis in neuroscience and neuroimaging. J. Neurosci. 35, 3293–3297 (2015).

44. Yu, Y. *et al.* Deep Dag Learning of Effective Brain Connectivity for FMRI Analysis. in 2023 *IEEE 20th International Symposium on Biomedical Imaging (ISBI)* 1–5 (IEEE, 2023).
45. Friston, K. J., Kahan, J., Biswal, B. & Razi, A. A DCM for resting state fMRI. Neuroimage 94, 396–407 (2014).
46. Crimi, A., Dodero, L., Sambataro, F., Murino, V. & Sona, D. Structurally constrained effective brain connectivity. Neuroimage 239, 118288 (2021).
47. Mellema, C. J. & Montillo, A. A. Novel machine learning approaches for improving the reproducibility and reliability of functional and effective connectivity from functional MRI. J. Neural Eng. 20, (2023).
48. Schwab, S. *et al.* Directed functional connectivity using dynamic graphical models. Neuroimage 175, 340–353 (2018).
49. Smith, S. M. *et al.* Network modelling methods for FMRI. Neuroimage 54, 875–891 (2011).
50. Gilson, M., Moreno-Bote, R., Ponce-Alvarez, A., Ritter, P. & Deco, G. Estimation of Directed Effective Connectivity from fMRI Functional Connectivity Hints at Asymmetries of Cortical Connectome. PLoS Comput. Biol. 12, e1004762 (2016).
51. Friston, K. Dynamic causal modeling and Granger causality Comments on: the identification of interacting networks in the brain using fMRI: model selection, causality and deconvolution. NeuroImage vol. 58 303–5; author reply 310-1 (2011).
52. David, O. fMRI connectivity, meaning and empiricism Comments on: Roebroeck et al. The identification of interacting networks in the brain using fMRI: model selection, causality and deconvolution. *NeuroImage* vol. 58 306–9; author reply 310-1 (2011).
53. Friston, K., Moran, R. & Seth, A. K. Analysing connectivity with Granger causality and dynamic causal modelling. Curr. Opin. Neurobiol. 23, 172–178 (2013).
54. Daunizeau, J., David, O. & Stephan, K. E. Dynamic causal modelling: a critical review of the biophysical and statistical foundations. Neuroimage 58, 312–322 (2011).
55. Allegra, M., Gilson, M. & Brovelli, A. Directed neural interactions in fMRI: a comparison between Granger Causality and Effective Connectivity. *bioRxiv* 2024.02.22.581068 (2024) doi:10.1101/2024.02.22.581068.
56. Razi, A. *et al.* Large-scale DCMs for resting-state fMRI. Netw Neurosci 1, 222–241 (2017).
57. Mäki-Marttunen, V., Diez, I., Cortes, J. M., Chialvo, D. R. & Villarreal, M. Disruption of transfer entropy and inter-hemispheric brain functional connectivity in patients with disorder of consciousness. Front. Neuroinform. 7, 24 (2013).
58. Costa, L. *et al.* Searching Multiregression Dynamic Models of Resting-State fMRI Networks Using Integer Programming. Bayesian Analysis 10, 441–478 (2015).
59. Xu, L. *et al.* A pooling-LiNGAM algorithm for effective connectivity analysis of fMRI data. Front. Comput. Neurosci. 8, 125 (2014).
60. Schaefer, A. *et al.* Local-Global Parcellation of the Human Cerebral Cortex from Intrinsic Functional Connectivity MRI. Cereb. Cortex 28, 3095–3114 (2018).

61. Glasser, M. F. *et al.* A multi-modal parcellation of human cerebral cortex. Nature 536, 171–178 (2016).
62. Schlösser, R. G. M. *et al.* Fronto-cingulate effective connectivity in major depression: a study with fMRI and dynamic causal modeling. Neuroimage 43, 645–655 (2008).
63. Sharaev, M. G., Zavyalova, V. V., Ushakov, V. L., Kartashov, S. I. & Velichkovsky, B. M. Effective Connectivity within the Default Mode Network: Dynamic Causal Modeling of Resting-State fMRI Data. Front. Hum. Neurosci. 10, 14 (2016).
64. Grefkes, C. *et al.* Modulating cortical connectivity in stroke patients by rTMS assessed with fMRI and dynamic causal modeling. Neuroimage 50, 233–242 (2010).
65. Mill, R. D., Bagic, A., Bostan, A., Schneider, W. & Cole, M. W. Empirical validation of directed functional connectivity. Neuroimage 146, 275–287 (2017).
66. Seguin, C., Razi, A. & Zalesky, A. Inferring neural signalling directionality from undirected structural connectomes. Nat. Commun. 10, 4289 (2019).
67. Frässle, S. *et al.* Whole-brain estimates of directed connectivity for human connectomics. Neuroimage 225, 117491 (2021).
68. Bastos, A. M. *et al.* Canonical microcircuits for predictive coding. Neuron 76, 695–711 (2012).
69. Shen, S. *et al.* Distinct organization of two cortico-cortical feedback pathways. Nat. Commun. 13, 6389 (2022).
70. Barron, H. C., Auksztulewicz, R. & Friston, K. Prediction and memory: A predictive coding account. Prog. Neurobiol. 192, 101821 (2020).
71. Mesulam, M. M. Principles of behavioral and cognitive neurology, 2nd ed. 2, 540 (2000).
72. Sancha-Velasco, A., Uceda-Heras, A. & García-Cabezas, M. Á. Cortical type: a conceptual tool for meaningful biological interpretation of high-throughput gene expression data in the human cerebral cortex. *Front. Neuroanat.* 17, (2023).
73. From Claude Bernard to Walter Cannon. Emergence of the concept of homeostasis. Appetite 51, 419–427 (2008).
74. Multivariate autoregressive modeling of fMRI time series. Neuroimage 19, 1477–1491 (2003).
75. Garnett, R. *Bayesian Optimization*. (Cambridge University Press, 2023).
76. Deco, G., Kringelbach, M. L., Jirsa, V. K. & Ritter, P. The dynamics of resting fluctuations in the brain: metastability and its dynamical cortical core. Sci. Rep. 7, 3095 (2017).
77. Milham, M. P. *et al.* An Open Resource for Non-human Primate Imaging. Neuron 100, 61–74.e2 (2018).
78. Friston, K. J. & Büchel, C. Attentional modulation of effective connectivity from V2 to V5/MT in humans. *Proc. Natl. Acad. Sci. U. S. A.* 97, 7591–7596 (2000).
79. Underwood, R., Tolmeijer, E., Wibroe, J., Peters, E. & Mason, L. Networks underpinning emotion: A systematic review and synthesis of functional and effective connectivity. Neuroimage 243, 118486 (2021).

80. Vezoli, J. *et al.* Cortical hierarchy, dual counterstream architecture and the importance of top-down generative networks. Neuroimage 225, 117479 (2021).
81. Covic, E. N. & Sherman, S. M. Synaptic properties of connections between the primary and secondary auditory cortices in mice. Cereb. Cortex 21, 2425–2441 (2011).
82. De Pasquale, R. & Sherman, S. M. Synaptic properties of corticocortical connections between the primary and secondary visual cortical areas in the mouse. J. Neurosci. 31, 16494–16506 (2011).
83. Javadzadeh, M. & Hofer, S. B. Dynamic causal communication channels between neocortical areas. Neuron 110, 2470–2483.e7 (2022).
84. Markov, N. T. *et al.* Anatomy of hierarchy: feedforward and feedback pathways in macaque visual cortex. J. Comp. Neurol. 522, 225–259 (2014).
85. Yeo, B. T. T. *et al.* The organization of the human cerebral cortex estimated by intrinsic functional connectivity. J. Neurophysiol. 106, 1125–1165 (2011).
86. Song, S., Sjöström, P. J., Reigl, M., Nelson, S. & Chklovskii, D. B. Highly nonrandom features of synaptic connectivity in local cortical circuits. PLoS Biol. 3, e68 (2005).
87. Ercsey-Ravasz, M. *et al.* A predictive network model of cerebral cortical connectivity based on a distance rule. Neuron 80, 184–197 (2013).
88. Hill, B. A simple general approach to inference about the tail of a distribution. Annals of Statistics 3, 1163–1174 (1975).
89. Klatzmann, U. *et al.* A connectome-based model of conscious access in monkey cortex. *bioRxiv* 2022.
    02.20.481230
    (2023) doi:10.1101/2022.02.20.481230.
90. Barone, P., Batardiere, A., Knoblauch, K. & Kennedy, H. Laminar distribution of neurons in extrastriate areas projecting to visual areas V1 and V4 correlates with the hierarchical rank and indicates the operation of a distance rule. J. Neurosci. 20, 3263–3281 (2000).
91. Pijnenburg, R. *et al.* Myelo- and cytoarchitectonic microstructural and functional human cortical atlases reconstructed in common MRI space. Neuroimage 239, 118274 (2021).
92. Campbell, A. W. Histological studies on the localisation of cerebral function. J. Ment. Sci. 50, 651–662 (1904).
93. Burt, J. B. *et al.* Hierarchy of transcriptomic specialization across human cortex captured by structural neuroimaging topography. Nat. Neurosci. 21, 1251–1259 (2018).
94. Barbas, H. Pattern in the laminar origin of corticocortical connections. J. Comp. Neurol. 252, 415–422 (1986).
95. Barbas, H. General cortical and special prefrontal connections: principles from structure to function. Annu. Rev. Neurosci. 38, 269–289 (2015).
96. Kringelbach, M. L., Perl, Y. S., Tagliazucchi, E. & Deco, G. Toward naturalistic neuroscience: Mechanisms underlying the flattening of brain hierarchy in movie-watching compared to rest and

task. Sci Adv 9, eade6049 (2023).

97. Molloy, K., Griffiths, T. D., Chait, M. & Lavie, N. Inattentional Deafness: Visual Load Leads to Time-Specific Suppression of Auditory Evoked Responses. J. Neurosci. 35, 16046–16054 (2015).
98. Choi, I., Demir, I., Oh, S. & Lee, S.-H. Multisensory integration in the mammalian brain: diversity and flexibility in health and disease. Philos. Trans. R. Soc. Lond. B Biol. Sci. 378, 20220338 (2023).
99. Chen, L., Cichy, R. M. & Kaiser, D. Alpha-frequency feedback to early visual cortex orchestrates coherent naturalistic vision. Sci Adv 9, eadi2321 (2023).
100. Khorsand, P., Moore, T. & Soltani, A. Combined contributions of feedforward and feedback inputs to bottom-up attention. Front. Psychol. 6, 155 (2015).
101. Debes, S. R. & Dragoi, V. Suppressing feedback signals to visual cortex abolishes attentional modulation. Science 379, 468–473 (2023).
102. Chen, W. G. *et al.* The Emerging Science of Interoception: Sensing, Integrating, Interpreting, and Regulating Signals within the Self. Trends Neurosci. 44, 3–16 (2021).
103. Seth, A. K. & Tsakiris, M. Being a Beast Machine: The Somatic Basis of Selfhood. Trends Cogn. Sci. 22, 969–981 (2018).
104. Hubel, D. H. & Wiesel, T. N. Receptive fields of single neurones in the cat’s striate cortex. J. Physiol. 148, 574–591 (1959).
105. Iwamura, Y. Hierarchical somatosensory processing. Curr. Opin. Neurobiol. 8, 522–528 (1998).
106. Rouiller, E. M., Simm, G. M., Villa, A. E., de Ribaupierre, Y. & de Ribaupierre, F. Auditory corticocortical interconnections in the cat: evidence for parallel and hierarchical arrangement of the auditory cortical areas. Exp. Brain Res. 86, 483–505 (1991).
107. Froudist-Walsh, S. *et al.* Gradients of neurotransmitter receptor expression in the macaque cortex. Nat. Neurosci. 26, 1281–1294 (2023).
108. Chaudhuri, R., Knoblauch, K., Gariel, M.-A., Kennedy, H. & Wang, X.-J. A Large-Scale Circuit Mechanism for Hierarchical Dynamical Processing in the Primate Cortex. Neuron 88, 419–431 (2015).
109. Hilgetag, C. C. & Goulas, A. ‘Hierarchy’ in the organization of brain networks. Philos. Trans. R. Soc. Lond. B Biol. Sci. 375, 20190319 (2020).
110. Crick, F. & Koch, C. Constraints on cortical and thalamic projections: the no-strong-loops hypothesis. Nature 391, 245–250 (1998).
111. Shao, Z. & Burkhalter, A. Different balance of excitation and inhibition in forward and feedback circuits of rat visual cortex. J. Neurosci. 16, 7353–7365 (1996).
112. Sherman, S. M. & Guillery, R. W. On the actions that one nerve cell can have on another: Distinguishing “drivers” from “modulators.” *Proceedings of the National Academy of Sciences* 95, 7121–7126 (1998).
113. Destexhe, A. Modelling corticothalamic feedback and the gating of the thalamus by the cerebral cortex. J. Physiol. Paris 94, 391–410 (2000).

114. Mayer, J., Schuster, H. G. & Claussen, J. C. Role of inhibitory feedback for information processing in thalamocortical circuits. Phys. Rev. E Stat. Nonlin. Soft Matter Phys. 73, 031908 (2006).
115. van Kerkoerle, T. *et al.* Alpha and gamma oscillations characterize feedback and feedforward processing in monkey visual cortex. *Proc. Natl. Acad. Sci. U. S. A.* 111, 14332–14341 (2014).
116. Li, W.-C., Soffe, S. R., Wolf, E. & Roberts, A. Persistent responses to brief stimuli: feedback excitation among brainstem neurons. J. Neurosci. 26, 4026–4035 (2006).
117. Yang, W., Carrasquillo, Y., Hooks, B. M., Nerbonne, J. M. & Burkhalter, A. Distinct balance of excitation and inhibition in an interareal feedforward and feedback circuit of mouse visual cortex. J. Neurosci. 33, 17373–17384 (2013).
118. Angelucci, A. & Petreanu, L. Feedforward and Feedback Connections: Functional Connectivity, Synaptic Physiology, and Function. in (Oxford University Press, 2023).
119. Weiler, S. *et al.* A primary sensory cortical interareal feedforward inhibitory circuit for tacto-visual integration. Nat. Commun. 15, 3081 (2024).
120. Zeki, S. M. The cortical projections of foveal striate cortex in the rhesus monkey. J. Physiol. 277, 227–244 (1978).
121. Zeki, S. & Shipp, S. The functional logic of cortical connections. Nature 335, 311–317 (1988).
122. Girard, P. & Bullier, J. Visual activity in area V2 during reversible inactivation of area 17 in the macaque monkey. J. Neurophysiol. 62, 1287–1302 (1989).
123. Girard, P., Salin, P. A. & Bullier, J. Visual activity in areas V3a and V3 during reversible inactivation of area V1 in the macaque monkey. J. Neurophysiol. 66, 1493–1503 (1991).
124. Girard, P., Salin, P. A. & Bullier, J. Visual activity in macaque area V4 depends on area 17 input. Neuroreport 2, 81–84 (1991).
125. Girard, P., Salin, P. A. & Bullier, J. Response selectivity of neurons in area MT of the macaque monkey during reversible inactivation of area V1. J. Neurophysiol. 67, 1437–1446 (1992).
126. Vezoli, J. *et al.* Quantitative analysis of connectivity in the visual cortex: extracting function from structure. Neuroscientist 10, 476–482 (2004).
127. Garrido, M. I., Kilner, J. M., Kiebel, S. J. & Friston, K. J. Evoked brain responses are generated by feedback loops. *Proc. Natl. Acad. Sci. U. S. A.* 104, 20961–20966 (2007).
128. Wacongne, C. *et al.* Evidence for a hierarchy of predictions and prediction errors in human cortex. *Proc. Natl. Acad. Sci. U. S. A.* 108, 20754–20759 (2011).
129. Desimone, R. Neural mechanisms for visual memory and their role in attention. *Proc. Natl. Acad. Sci. U. S. A.* 93, 13494–13499 (1996).
130. Murray, S. O., Kersten, D., Olshausen, B. A., Schrater, P. & Woods, D. L. Shape perception reduces activity in human primary visual cortex. *Proc. Natl. Acad. Sci. U. S. A.* 99, 15164–15169 (2002).
131. Harrison, L. M., Stephan, K. E., Rees, G. & Friston, K. J. Extra-classical receptive field effects measured in striate cortex with fMRI. Neuroimage 34, 1199–1208 (2007).

132. Barceló, F., Suwazono, S. & Knight, R. T. Prefrontal modulation of visual processing in humans. Nat. Neurosci. 3, 399–403 (2000).

133. Shine, J. M. Neuromodulatory control of complex adaptive dynamics in the brain. Interface Focus 13, 20220079 (2023).

134. Shine, J. M., Lewis, L. D., Garrett, D. D. & Hwang, K. The impact of the human thalamus on brain-wide information processing. Nat. Rev. Neurosci. 24, 416–430 (2023).

135. Patow, G., Martin, I., Sanz Perl, Y., Kringelbach, M. L. & Deco, G. Whole-brain modelling: an essential tool for understanding brain dynamics. Nature Reviews Methods Primers 4, 1–2 (2024).

136. Wang, H. E. *et al.* Delineating epileptogenic networks using brain imaging data and personalized modeling in drug-resistant epilepsy. Sci. Transl. Med. 15, eabp8982 (2023).

137. Demirtaş, M. *et al.* Hierarchical Heterogeneity across Human Cortex Shapes Large-Scale Neural Dynamics. Neuron 101, 1181–1194.e13 (2019).

138. Wang, P. *et al.* Inversion of a large-scale circuit model reveals a cortical hierarchy in the dynamic resting human brain. Sci Adv 5, eaat7854 (2019).

139. Murray, J. D., Demirtaş, M. & Anticevic, A. Biophysical Modeling of Large-Scale Brain Dynamics and Applications for Computational Psychiatry. Biol Psychiatry Cogn Neurosci Neuroimaging 3, 777–787 (2018).

140. Deco, G. *et al.* Resting-state functional connectivity emerges from structurally and dynamically shaped slow linear fluctuations. J. Neurosci. 33, 11239–11252 (2013).

141. Mejias, J. F., Murray, J. D., Kennedy, H. & Wang, X.-J. Feedforward and feedback frequency-dependent interactions in a large-scale laminar network of the primate cortex. Sci Adv 2, e1601335 (2016).

142. Joglekar, M. R., Mejias, J. F., Yang, G. R. & Wang, X.-J. Inter-areal Balanced Amplification Enhances Signal Propagation in a Large-Scale Circuit Model of the Primate Cortex. Neuron 98, 222–234.e8 (2018).

143. Mejías, J. F. & Wang, X.-J. Mechanisms of distributed working memory in a large-scale network of macaque neocortex. Elife 11, (2022).

144. Pang, J. C. *et al.* Geometric constraints on human brain function. Nature (2023) doi:10.1038/s41586-023-06098-1.

145. Faskowitz, J. *et al.* Commentary on Pang et al. (2023)*Nature*. *bioRxiv* 2023.
07.20.549785
(2023) doi:10.1101/2023.07.20.549785.

146. Patil, K. R., Jung, K. & Eickhoff, S. B. Commentary on Pang et al. (2023) Nature. *bioRxiv* 2023.10.06.561240 (2023) doi:10.1101/2023.10.06.561240.

147. Friston, K. J., Harrison, L. & Penny, W. Dynamic causal modelling. Neuroimage 19, 1273–1302 (2003).

148. Ji, J. *et al.* A survey on brain effective connectivity network learning. IEEE Trans. Neural Netw. Learn. Syst. 34, 1879–1899 (2023).
149. Khan, D. M., Yahya, N., Kamel, N. & Faye, I. A novel method for efficient estimation of brain effective connectivity in EEG. Comput. Methods Programs Biomed. 228, 107242 (2023).
150. Zou, A., Ji, J., Lei, M., Liu, J. & Song, Y. Exploring Brain Effective Connectivity Networks Through Spatiotemporal Graph Convolutional Models. IEEE Trans Neural Netw Learn Syst PP, (2022).
151. Gurbuz, M. B. & Rekik, I. Deep Graph Normalizer: A geometric deep learning approach for estimating connectional brain templates. *arXiv [cs.CV]* (2020).
152. He, K. *et al.* Transformers in medical image analysis. Intell. Med. 3, 59–78 (2023).
153. Bessadok, A., Mahjoub, M. A. & Rekik, I. Graph neural networks in network neuroscience. 45, 5833–5848 (2022).
154. Shine, J. M., Aburn, M. J., Breakspear, M. & Poldrack, R. A. The modulation of neural gain facilitates a transition between functional segregation and integration in the brain. Elife 7, (2018).
155. O’Callaghan, C., Walpola, I. C. & Shine, J. M. Neuromodulation of the mind-wandering brain state: the interaction between neuromodulatory tone, sharp wave-ripples and spontaneous thought. Philos. Trans. R. Soc. Lond. B Biol. Sci. 376, 20190699 (2021).
156. Munn, B. R., Müller, E. J., Wainstein, G. & Shine, J. M. The ascending arousal system shapes neural dynamics to mediate awareness of cognitive states. Nat. Commun. 12, 6016 (2021).
157. Li, M. *et al.* Transitions in information processing dynamics at the whole-brain network level are driven by alterations in neural gain. PLoS Comput. Biol. 15, e1006957 (2019).
158. Deco, G. *et al.* Dynamical consequences of regional heterogeneity in the brain’s transcriptional landscape. Sci. Adv. 7, eabf4752 (2021).
159. Zhang, S. *et al.* In vivo whole-cortex marker of excitation-inhibition ratio indexes cortical maturation and cognitive ability in youth. *Proc. Natl. Acad. Sci. U. S. A.* 121, e2318641121 (2024).
160. Kim, Y. *et al.* Brain-wide maps reveal stereotyped cell-type-based cortical architecture and subcortical sexual dimorphism. Cell 171, 456–469.e22 (2017).
161. Ullman, S. Sequence seeking and counter streams: a computational model for bidirectional information flow in the visual cortex. Cereb. Cortex 5, 1–11 (1995).
162. Autio, J. A. *et al.* Towards HCP-Style macaque connectomes: 24-Channel 3T multi-array coil, MRI sequences and preprocessing. Neuroimage 215, 116800 (2020).
163. Smith, S. M. *et al.* Resting-state fMRI in the Human Connectome Project. Neuroimage 80, 144–168 (2013).
164. Hanke, M. *et al.* A studyforrest extension, simultaneous fMRI and eye gaze recordings during prolonged natural stimulation. Sci Data 3, 160092 (2016).
165. Lee, J.-J., Lee, S., Lee, D. H. & Woo, C.-W. Functional brain reconfiguration during sustained pain. Elife 11, (2022).

166. Lee, J.-J. *et al.* A neuroimaging biomarker for sustained experimental and clinical pain. Nat. Med. 27, 174–182 (2021).
167. Salimi-Khorshidi, G. *et al.* Automatic denoising of functional MRI data: combining independent component analysis and hierarchical fusion of classifiers. Neuroimage 90, 449–468 (2014).
168. Pruim, R. H. R. *et al.* ICA-AROMA: A robust ICA-based strategy for removing motion artifacts from fMRI data. Neuroimage 112, 267–277 (2015).
169. Sotiropoulos, S. N. *et al.* Advances in diffusion MRI acquisition and processing in the Human Connectome Project. Neuroimage 80, 125–143 (2013).
170. Setsompop, K. *et al.* Pushing the limits of in vivo diffusion MRI for the Human Connectome Project. Neuroimage 80, 220–233 (2013).
171. Tournier, J.-D. *et al.* MRtrix3: A fast, flexible and open software framework for medical image processing and visualisation. Neuroimage 202, 116137 (2019).
172. Tournier, J.-D., Calamante, F., Gadian, D. G. & Connelly, A. Direct estimation of the fiber orientation density function from diffusion-weighted MRI data using spherical deconvolution. Neuroimage 23, 1176–1185 (2004).
173. Jeurissen, B., Tournier, J.-D., Dhollander, T., Connelly, A. & Sijbers, J. Multi-tissue constrained spherical deconvolution for improved analysis of multi-shell diffusion MRI data. Neuroimage 103, 411–426 (2014).
174. Yeh, F.-C., Verstynen, T. D., Wang, Y., Fernández-Miranda, J. C. & Tseng, W.-Y. I. Deterministic diffusion fiber tracking improved by quantitative anisotropy. PLoS One 8, e80713 (2013).
175. Smith, R. E., Tournier, J.-D., Calamante, F. & Connelly, A. SIFT2: Enabling dense quantitative assessment of brain white matter connectivity using streamlines tractography. Neuroimage 119, 338–351 (2015).
176. Zalesky, A. *et al.* Connectome sensitivity or specificity: which is more important? *Neuroimage* 142, 407–420 (2016).
177. Rubinov, M. & Sporns, O. Complex network measures of brain connectivity: uses and interpretations. Neuroimage 52, 1059–1069 (2010).
178. Modha, D. S. & Singh, R. Network architecture of the long-distance pathways in the macaque brain. *Proc. Natl. Acad. Sci. U. S. A.* 107, 13485–13490 (2010).
179. Petersen, S. E., Seitzman, B. A., Nelson, S. M., Wig, G. S. & Gordon, E. M. Principles of cortical areas and their implications for neuroimaging. Neuron (2024) doi:10.1016/j.neuron.2024.05.008.
180. Ji, J. L. *et al.* Mapping the human brain's cortical-subcortical functional network organization. Neuroimage 185, 35–57 (2019).
181. Barnett, L., Barrett, A. B. & Seth, A. K. Granger causality and transfer entropy are equivalent for Gaussian variables. Phys. Rev. Lett. 103, 238701 (2009).
182. Behrendt, S., Dimpfl, T., Peter, F. J. & Zimmermann, D. J. RTransferEntropy — Quantifying information flow between different time series using effective transfer entropy. SoftwareX 10, 100265 (2019).

183. Luppi, A. I. *et al.* Systematic evaluation of fMRI data-processing pipelines for consistent functional connectomics. Nat. Commun. 15, 4745 (2024).

184. Hlinka, J., Palus, M., Vejmelka, M., Mantini, D. & Corbetta, M. Functional connectivity in resting-state fMRI: is linear correlation sufficient? *Neuroimage* 54, 2218–2225 (2011).

185. Nozari, E. *et al.* Macroscopic resting-state brain dynamics are best described by linear models. Nat Biomed Eng 8, 68–84 (2024).

186. Barnett, L. & Seth, A. K. The MVGC multivariate Granger causality toolbox: a new approach to Granger-causal inference. J. Neurosci. Methods 223, 50–68 (2014).

187. Daunizeau, J., Stephan, K. E. & Friston, K. J. Stochastic dynamic causal modelling of fMRI data: should we care about neural noise? *Neuroimage* 62, 464–481 (2012).

188. Buhlmann, P. & van de Geer, S. *Statistics for High-Dimensional Data: Methods, Theory and Applications*. (Springer, Berlin, Germany, 2011).

189. Deco, G., Vidaurre, D. & Kringelbach, M. L. Revisiting the global workspace orchestrating the hierarchical organization of the human brain. Nat. Hum. Behav. 5, 497–511 (2021).

190. Deco, G. *et al.* Different hierarchical reconfigurations in the brain by psilocybin and escitalopram for depression. Nat. Ment. Health 1–15 (2024).

191. Economo, C., Koskinas, G. N. & Triarhou, L. Atlas of cytoarchitectonics of the adult Human Cerebral Cortex. (2008).

Figures

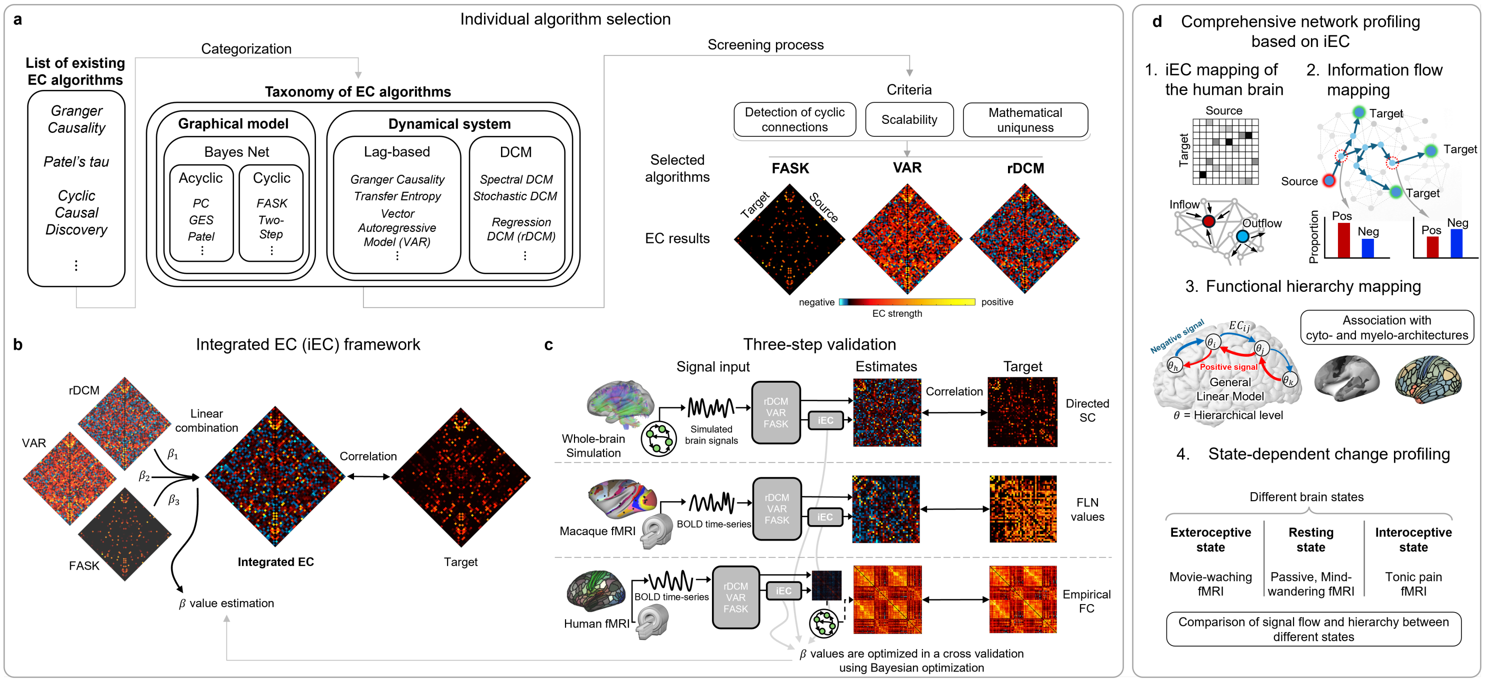

Figure 1

Overview of the iEC approach and comprehensive network profiling of the human brain.

a, Taxonomy of EC algorithms. We categorized individual EC algorithms into two major groups, one based on “Graphical model” and the other based on “Dynamical system”, and selected representative EC algorithms for each category through a dedicated screening process. The final chosen algorithms were FASK, VAR and rDCM. **b**, The individual algorithms were then combined using a linear integration technique, which performs a weighted sum of their EC results to create an iEC. **c**, Both individual and iEC algorithms were evaluated through a three-step validation process involving: *i)* inputting either simulated (top: whole-brain simulation) or empirical BOLD signals (middle and bottom: macaque and human fMRI) into each algorithm, *ii)*estimating EC or ‘simulated FC’ matrices, and *iii)* quantitatively comparing the resulting matrices to their corresponding targets – *i.e.*, synthetic directed SC [top], tract-tracing based ‘Fraction of Labeled Neuron’ (FLN) values [middle], empirical FC [bottom] – to assess validity. **d**, After methodological validation, the group-level iEC map from empirical human fMRI was profiled in terms of (1) degree distribution and (2) signal flow across the networks. Finally, (3) the hierarchical levels of the whole brain areas were estimated using a general linear model based on iEC values and (4) compared across different brain states including exteroceptive, resting and interoceptive states.

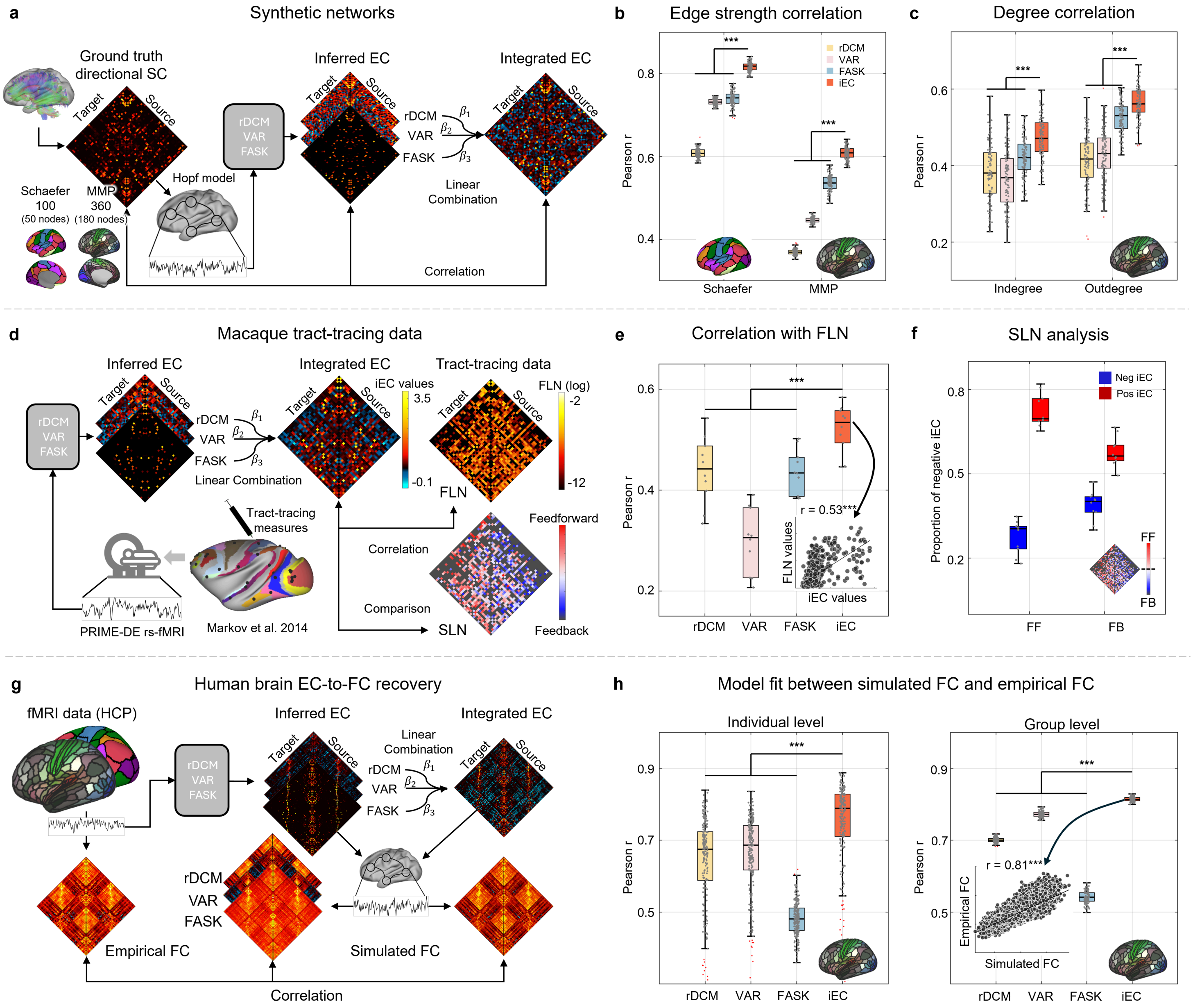

Figure 2

Validation of individual and integrated EC algorithms.

a, Validation using synthetic directed networks. Using diffusion MRI from the HCP dataset, we first constructed a structural connectivity (SC) matrix at two different resolutions: Schaefer-100[60] and MMP-360[61]. To induce directionality, the cells in this matrix were randomly shuffled while preserving each node’s outdegree. This directed SC served as the ground truth connectivity matrix of the Hopf model to generate brain signals, which were then fed into the individual EC algorithms. The resulting ECs were integrated to construct the iEC matrix. We then measured the correlation between the identified ECs and ground truths (*i.e.,* synthetic networks generated across 100 iterations) using two metrics (**b**, **c**; see **Supplementary Fig. 2** for results from the Schaefer atlas). **d**, Validation using macaque tract-tracing data. Individual ECs were first inferred from fMRI data of anesthetized macaques, using data extracted from 40 tracer-injected sites. We then measured the correlation between the ECs and the fraction of labeled neurons (FLN). **e**, Correlation between ECs and FLN at the individual level. The inset shows a scatter plot for median correlation value. **f**, Next, using supragranular labeled neurons (SLN), connections were categorized into feedforward (FF) and feedback (FB) pathways (based on 0.5-cutoff for SLN), and the iEC of these two pathways were separately profiled. **g**, EC-to-FC recovery analysis in the human brain. Individual ECs were derived from resting-state fMRI data and used to construct the iEC. Next, each EC was fed as a connectivity matrix to the Hopf model to simulate brain signals, which were subsequently used to reconstruct FC. This reconstructed FC was then compared to the empirical FC (thus called “*EC-to-FC recovery*”). **h**, The correlation between simulated and empirical FCs at the individual level (left) and group level (right).

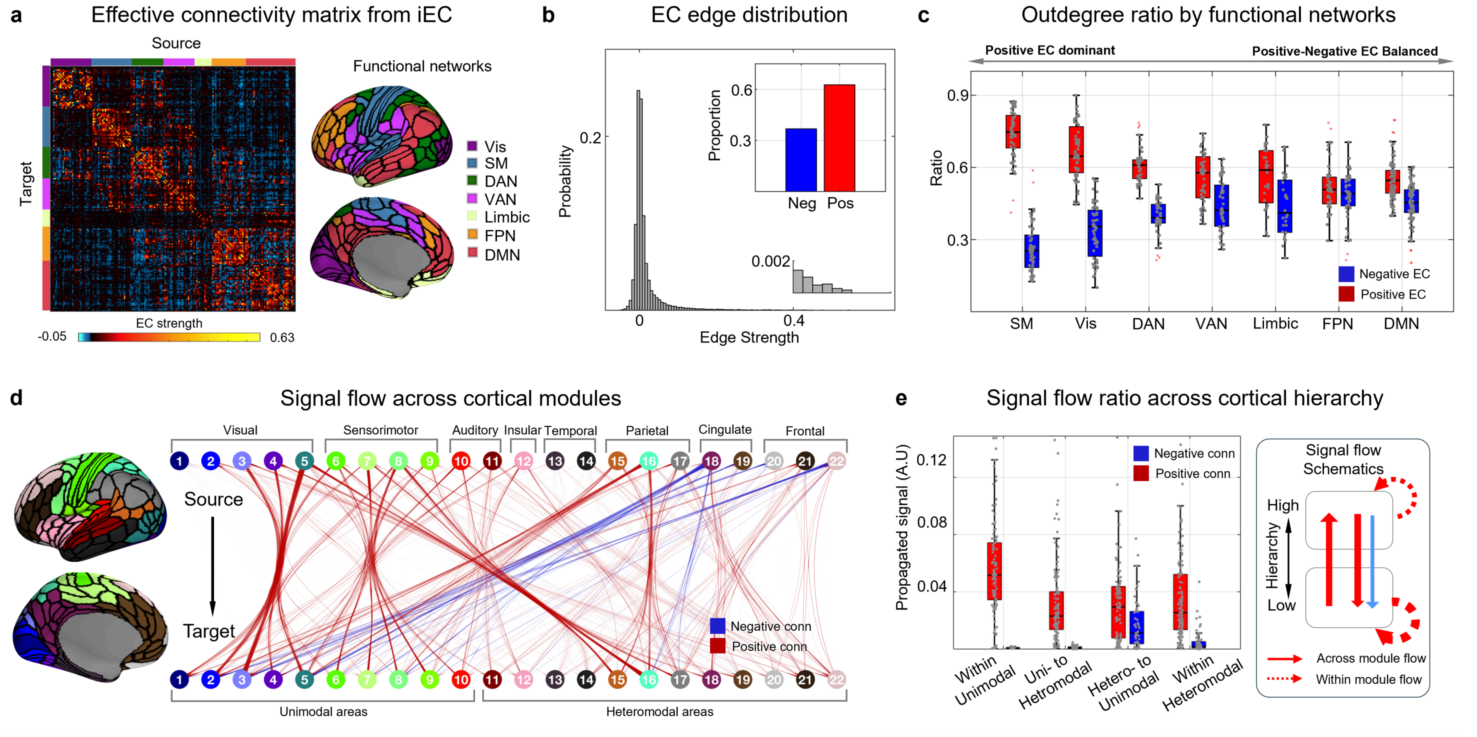

Figure 3

The iEC profiling of the resting-state human brain

a, The modular structure of iEC is unveiled by organizing it according to 7 functional networks from the Yeo-Krienen atlas[85] (for visualization purpose, only the left cortex presented). **b**, The edge distribution of iEC shows a characteristic heavy-tail distribution. **c**, Profiling of the positive-negative ratio of outdegree connections (see **Supplementary Fig. 5** for the indegree plot) based on the 7 functional networks. Note that the dichotomized pattern between positive and negative connections in the unimodal regions gradually converges into a form with a more balanced ratio in higher order heteromodal areas. **d**, Signal propagation based on a linear dynamical system[16] across 22 modules of the MMP-360 atlas. Modules are categorized into functionally specialized subnetworks for easier interpretation of the signal flow patterns. Edge thickness indicates signal strength, and color represents positive (red) and negative (blue) signal flows, respectively. **e**, Stratification of signal propagation based on the proportion of positive and negative signal flows within/between unimodal and heteromodal systems. Positive signal flow prevails within and between the systems, whereas negative signal flow is primarily observed in hetero-to-unimodal pathways during resting-state fMRI.

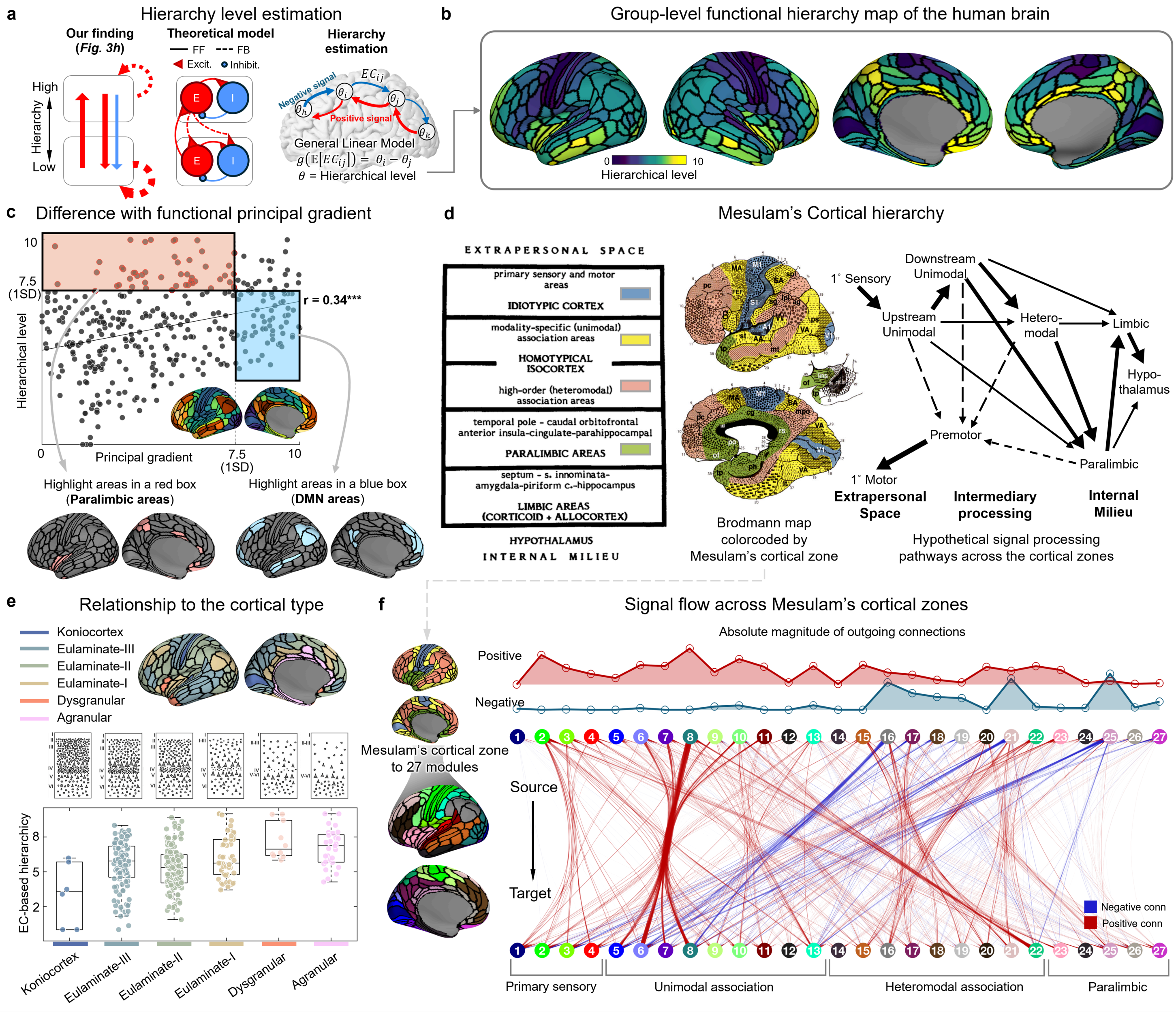

Figure 4

The iEC framework reveals a characteristic structure of signal flow hierarchy in the human brain

a, Schematic of our approach to estimating the hierarchy. To illustrate the process of hierarchy estimation, we put in side by side a hierarchical signal flow from our previous findings (**Fig. 3h**) and its corresponding theoretical circuit model. Given that the connection topology in the macaque study (represented by SLN) was used to estimate cortical hierarchy, here, we replaced the SLN with our iEC matrix to infer the hierarchy level of each cortical area across the entire brain. **b**, The resultant signal flow hierarchy map is shown. The insular and paralimbic areas are positioned at the top of the hierarchy, while the primary sensorimotor areas are located at the bottom. **c**, The difference between our EC-based hierarchy and FC-based functional gradient. The brain areas with higher EC-based hierarchy (>mean+1SD) but lower functional gradient (<mean-1SD) are marked by red, while those with opposite

profiles are marked by blue (*i.e.,* higher gradient but lower hierarchy) in both graphs and cortical surfaces. **d**, The cortical zones proposed by Mesulam[71] (left), indicating different levels of cortical hierarchy. Note that except for subcortical limbic areas (which were not included in the current study; see **Discussion** related to the study's limitation), the paralimbic areas are at the top of the hierarchy within the neocortex. These four zones are superimposed on the Brodmann parcellation scheme (middle). Finally, the hypothetical signal processing pathways across corresponding hierarchical levels proposed by Mesulam are shown (right). All figures are sourced from Mesulam, 2000[71]. **e,** The relationship between the identified signal flow hierarchy and histological cortical types. Note that as the hierarchical value increases, the cortical type transitions from a laminar structure with clearly defined granular layers to one with less distinct or even absent granular layers. **f**, Signal propagation was analyzed across 27 modules derived from Mesulam's cortical zones. Positive signals predominantly originated from primary and unimodal association areas and decreased along the hierarchy, while the negative signals progressively increase as they move from primary sensory to paralimbic areas.

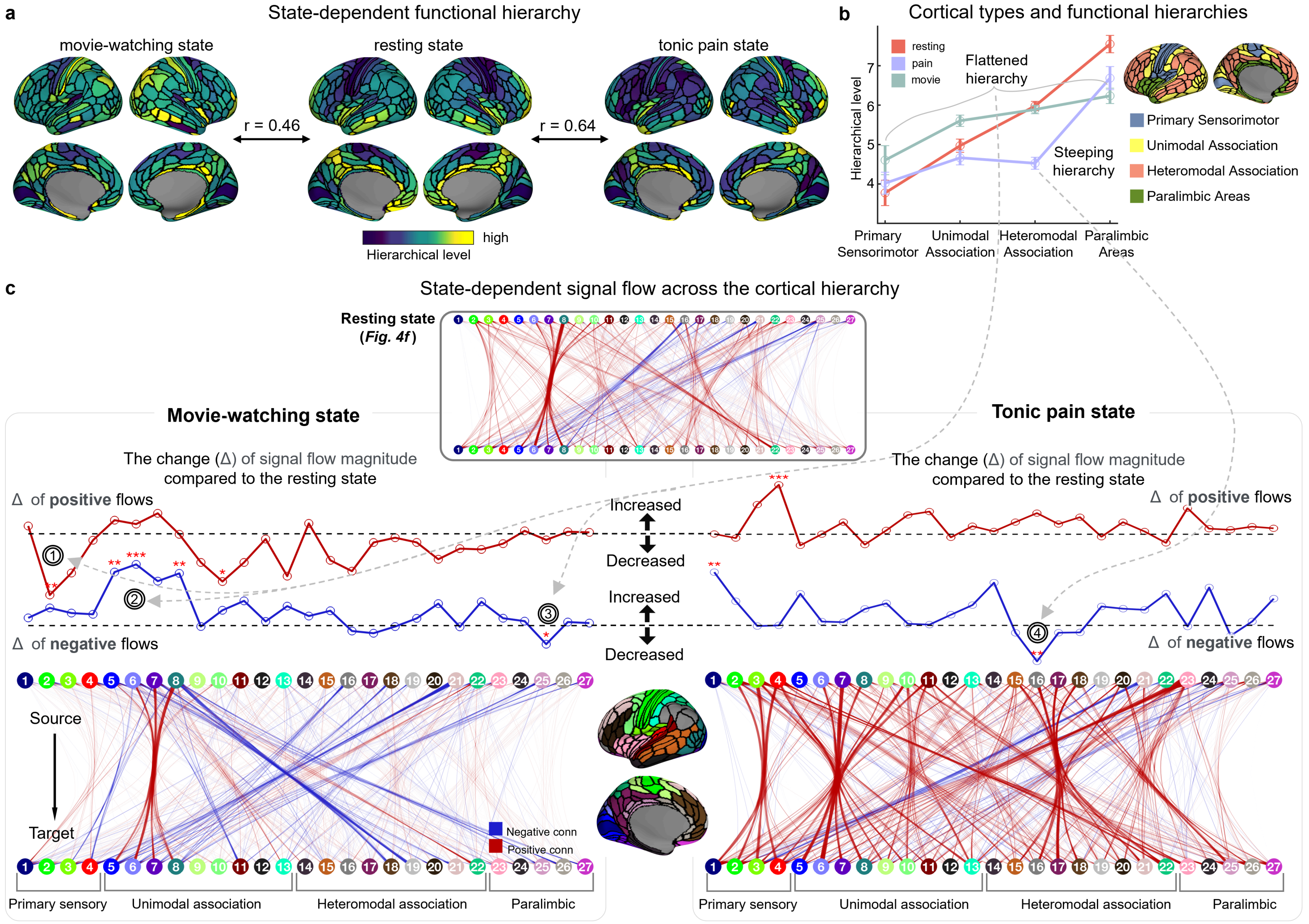

Figure 5

State-dependent reorganization of signal flow hierarchy and signal flow of the human brain

a, Signal flow hierarchy maps derived from movie-watching (left), resting (middle) and tonic pain (right) states. The correlations of their spatial patterns are shown. **b**, State-dependent changes in hierarchy levels sorted out based on the Mesulam's four cortical zones (*i.e.,* primary sensorimotor, unimodal association, heteromodal association, and paralimbic areas). Note that the movie-watching state resulted in a flattened cortical hierarchy, while the tonic pain condition accentuated the disparity between paralimbic and non-paralimbic areas (steepening hierarchy). **c**, Signal flow analysis across 27 modules of MMP (parcellated according to the cortical zones) in the movie-watching and tonic pain states. (Upper) The magnitude of changes in signal flows (Δ) in these states compared to the resting state were presented as a line graph, separately for positive and negative streams and statistically tested (***: $p_{FDR} < 0.05$, **: $p<0.025$, *: $p< 0.05$). In the graph, the findings of ☒ 'decreased positive signal flow' and ☒ 'increased negative signal flow' are both related to enhanced hierarchy at the primary sensory and visual association areas, while ☒ 'decreased negative signal flow' implicates diminished hierarchy of the paralimbic regions, which collectively induce the whole-brain hierarchy to flatten during a movie-watching state. Similarly, ☒ 'decreased negative signal flow' in the default mode area means its diminished hierarchy during a tonic pain condition, which may cause the steepening hierarchy in this brain state. (Bottom) The edge-bundling visualization presenting overall signal flows qualitatively supports these statistical results.

Supplementary Files

This is a list of supplementary files associated with this preprint. Click to download.

- OhYHetaliECsupplementary.docx